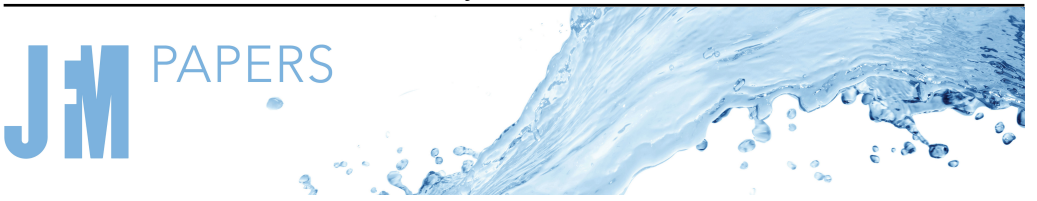
J. Fluid Mech. (2025), *vol.* 1025, A37, doi:10.1017/jfm.2025.10934



Evolution of perturbed long nonlinear plane, ring, and hybrid surface waves

Benjamin Martin[1], **Dmitri Tseluiko**[1] **and Karima Khusnutdinova**[1]

[1]Department of Mathematical Sciences, Loughborough University, Loughborough LE11 3TU, UK

Corresponding author: Karima Khusnutdinova, k.khusnutdinova@lboro.ac.uk

(Received 17 May 2025; revised 18 October 2025; accepted 29 October 2025)

The two-dimensional (2-D) evolution of perturbed long weakly nonlinear surface plane, ring and hybrid waves, consisting, to leading order, of a part of a ring and two tangent plane waves, is modelled numerically within the scope of the 2-D Boussinesq–Peregrine system. Numerical runs are initiated and interpreted using the reduced 2-D cylindrical Korteweg–de Vries (cKdV)-type and Kadomtsev–Petviashvili II (KPII) equations. The cKdV-type equation leads to two different models, the KdVθ, where θ stands for a polar angle, and cKdV equations, depending on whether we use the general or singular (i.e. the envelope of the general) solution of the associated nonlinear first-order differential equation. The KdVθ equation is also derived directly from the 2-D Boussinesq–Peregrine system and used to analytically describe the intermediate 2-D asymptotics of line solitons subject to sufficiently long transverse perturbations of finite strength, while the cKdV equation is used to initiate outward- and inward-propagating ring waves with localised and periodic perturbations. Both of these equations, together with the KPII equation, are used to model the evolution of hybrid waves, where we show, in particular, that large localised waves (lumps) can appear as transient (emerging and then disappearing) states in the evolution of inward-propagating waves, contributing to the possible mechanisms for the generation of rogue waves. Detailed comparisons are made between the key features of the non-stationary 2-D modelling and relevant predictions of the reduced equations.

Key words: surface gravity waves, shallow water flows, nonlinear instability

1. Introduction

Synthetic aperture radar (SAR) images of the waves generated in narrow straits and river–sea interaction areas often look like a part of a ring wave with two attached tangent plane waves (see, for example, figure 1 for the image of a hybrid wave generated in the Strait

© The Author(s), 2025. Published by Cambridge University Press. This is an Open Access article, distributed under the terms of the Creative Commons Attribution licence (https://creativecommons.org/licenses/by/4.0/), which permits unrestricted re-use, distribution and reproduction, provided the original article is properly cited.

https://doi.org/10.1017/jfm.2025.10934 Published online by Cambridge University Press



Figure 1. Hybrid wave generated in the Strait of Gibraltar (Terra MODIS, 22 May 2017, 11:30 UTC. NASA ESDIS Worldview, https://user.eumetsat.int/resources/case-studies/internal-waves-in-the-eastern-strait-of-gibraltar).

of Gibraltar). To the best of our knowledge, the first mentioning of the possibility of the existence of stable outward-propagating hybrid waves in theoretical literature was due to Ostrovskii & Shrira (1976), who also predicted, using ray theory, that inward-propagating hybrid waves are unstable. However, there have been no attempts to systematically model the evolution of such two-dimensional (2-D) waves. This raises several key questions. Does numerical modelling support their existence? Is there indeed any difference between the outward and inward propagation? If there is some non-trivial evolution scenario in the latter case, will its key features persist under perturbations? It is also important to determine, which theoretical framework can be used to initiate the wave and interpret the features observed in numerical runs. Hence, the primary aim of our study is the 2-D modelling of the propagation and evolution of both outward- and inward-propagating hybrid waves, which, in this first study on the topic, is performed within the scope of the 2-D Boussinesq–Peregrine (Peregrine 1967) system for surface waves in a homogeneous fluid. However, we also outline how theoretical considerations can be extended to the general setting of surface and internal waves in a stratified fluid on a parallel shear flow.

In order to initiate the numerical runs and interpret their results, we use approaches based on asymptotic multiple-scales expansions describing weakly nonlinear plane and ring waves, and their 2-D extensions. Naturally, since we view the hybrid waves as a combination of the elements of plane and ring waves (at least initially), we also model the evolution of the perturbed plane and ring waves *per se*. Approaching the plane waves from a new perspective allows us to derive a new amplitude equation (which we call the KdVθ equation, where θ stands for the polar angle), which is used to obtain analytical results for plane waves subject to long transverse perturbations. We also model the evolution of 2-D perturbations of ring waves. Different aspects of the stability of ring waves is a topic

https://doi.org/10.1017/jfm.2025.10934 Published online by Cambridge University Press

of active current research (see Khusnutdinova 2020; Hooper, Khusnutdinova & Grimshaw 2021; Krechetnikov 2024; Zhang *et al.* 2024; Hornick, Pelinovsky & Schneider 2025 and the references therein).

The weakly nonlinear theory for plane waves leading to the Korteweg–de Vries (KdV) equation and its extensions are an important theoretical framework that allows one to understand and interpret many features of the behaviour of both surface and internal plane waves in the ocean (see, for example, Grimshaw *et al.* 1998; Grimshaw 2005; Lamb 2005; Grue 2006; Helfrich & Melville 2006; Apel *et al.* 2007; Bona, Lannes & Saut 2008; Grimshaw *et al.* 2010; Ablowitz & Baldwin 2012; Grimshaw, Helfrich & Johnson 2013; Chakravarty & Kodama 2014; Ostrovsky *et al.* 2015; Stastna 2022; Sidorovas *et al.* 2024 and references therein). Derivation of the KdV equation in the general setting of a stratified fluid with a parallel depth-dependent shear flow is based on the existence of the modal decomposition in the set of Euler equations with boundary conditions appropriate for oceanographic applications. In this decomposition, the leading-order vertical particle displacement ζ (with $w = \mathrm{d}\zeta/\mathrm{d}t$ defining the vertical velocity) is given by

$$\zeta = A(T, \tilde{\xi})\phi(z), \tag{1.1}$$

where $A(T, \tilde{\xi})$ is the amplitude function satisfying the KdV equation ($T = \epsilon t, \tilde{\xi} = x - c_0 t$, where c_0 is the linear long-wave speed of plane waves propagating in the x direction, ϵ is the small-amplitude parameter) and $\phi(z)$ is the modal function that should be found from the set of appropriate modal equations (for details, see, e.g., Grimshaw 2005 and references therein).

In contrast to this well-developed theory, asymptotic theory describing long surface ring waves in a homogeneous fluid propagating over a parallel depth-dependent shear flow was developed relatively recently by Johnson (1990). The theory was generalised to describe long surface and internal ring waves in a stratified fluid with the density $\rho_0(z)$ and a parallel depth-dependent shear flow $u_0(z)$ by Khusnutdinova & Zhang (2016). The generalisation was based on finding a new far-field modal decomposition in the set of Euler equations, more complicated than that for plane waves. In particular, rather than (1.1), the leading-order vertical particle displacement for the ring waves is given by

$$\zeta = A(R, \xi, \theta)\phi(z, \theta), \tag{1.2}$$

where r, θ are polar coordinates in the reference frame moving at a constant speed c, $R = \epsilon r k(\theta)$ is a slow variable, $\xi = r k(\theta) - st$ is a fast variable, s is the wave speed in the absence of any shear flow, $k(\theta)$ is a function accounting for the effect of a shear flow on the linear long-wave speed in different directions and ϵ is again the small-amplitude parameter. In non-dimensional variables, the bottom is at $z = 0$, the unperturbed free surface is at $z = 1$.

For the given density $\rho_0(z)$ and shear flow $u_0(z)$, the modal function $\phi(z, \theta)$, the function $k(\theta)$ and admissible wave speeds s should be found by solving the boundary-value problem (modal equations)

$$\left(\frac{\rho_0 F^2}{k^2 + k'^2}\phi_z\right)_z - \rho_{0z}\phi = 0 \quad \text{for} \quad 0 < z < 1, \tag{1.3}$$

$$\frac{F^2}{k^2 + k'^2}\phi_z - \phi = 0 \quad \text{at} \quad z = 1, \tag{1.4}$$

$$\phi = 0 \quad \text{at} \quad z = 0, \tag{1.5}$$

$$\text{where} \quad k' = \frac{\mathrm{d}k}{\mathrm{d}\theta} \quad \text{and} \quad F = -s + (u_0 - c)(k\cos\theta - k'\sin\theta), \tag{1.6}$$

and the natural choice of the constant c is the speed of the flow at the bottom, i.e. $c = u_0(0)$.

https://doi.org/10.1017/jfm.2025.10934 Published online by Cambridge University Press

The amplitude equation has the form

$$\mu_1 A_R + \mu_2 A A_\xi + \mu_3 A_{\xi\xi\xi} + \mu_4 \frac{A}{R} + \mu_5 \frac{A_\theta}{R} = 0, \tag{1.7}$$

where the coefficients are given by

$$\mu_1 = 2s \int_0^1 \rho_0 F \phi_z^2 \, \mathrm{d}z, \quad \mu_2 = -3 \int_0^1 \rho_0 F^2 \phi_z^3 \, \mathrm{d}z, \quad \mu_3 = -(k^2 + k'^2) \int_0^1 \rho_0 F^2 \phi^2 \, \mathrm{d}z, \tag{1.8}$$

$$\mu_4 = -\int_0^1 \left\{ \frac{\rho_0 \phi_z^2 k (k + k'')}{(k^2 + k'^2)^2} \big[(k^2 - 3k'^2) F^2 - 4k'(k^2 + k'^2)(u_0 - c) \sin\theta F \right.$$

$$\left. - \sin^2\theta (u_0 - c)^2 (k^2 + k'^2)^2 \big] + \frac{2\rho_0 k}{k^2 + k'^2} F \phi_z \phi_{z\theta} [k' F + (k^2 + k'^2)(u_0 - c) \sin\theta] \right\} \mathrm{d}z, \tag{1.9}$$

$$\mu_5 = -\frac{2k}{k^2 + k'^2} \int_0^1 \rho_0 F \phi_z^2 \big[k' F + (u_0 - c)(k^2 + k'^2) \sin\theta \big] \, \mathrm{d}z. \tag{1.10}$$

For the particular case of surface waves in a homogeneous fluid with the non-dimensional density $\rho_0 = 1$, we have the following solution of the modal equation (1.3) with the boundary condition (1.5):

$$\phi = \Lambda \big(k^2 + k'^2\big) \int_0^z \frac{1}{F^2} \, \mathrm{d}z. \tag{1.11}$$

Here Λ is a parameter. Next, assuming that $u_0(z) = 0$ (no shear flow), setting $k = 1$ and $s = 1$ (concentric wavefronts, non-dimensional wave speed), the boundary condition (1.4) yields $\Lambda = 1$, while in the presence of the shear flow we recover, from the same boundary condition, the 'generalised Burns condition' (Johnson 1990)

$$\big(k^2 + k'^2\big) \int_0^1 \frac{1}{F^2} \, \mathrm{d}z = 1, \tag{1.12}$$

while the modal function is given by

$$\phi = \big(k^2 + k'^2\big) \int_0^z \frac{1}{F^2} \, \mathrm{d}z. \tag{1.13}$$

Equation (1.12) is a nonlinear first-order ordinary differential equation (ODE) that admits both the general solution (one-parameter family of solutions) and the singular solution – an additional solution, given by the envelope of the general solution (see Johnson 1990 and references therein). The general solution of (1.12) is dependent on a single constant parameter a and has the form

$$k(\theta; a) = a \cos\theta + b(a) \sin\theta, \quad \text{where} \quad \big[a^2 + b(a)^2\big] \int_0^1 \frac{\mathrm{d}z}{[1 - (u_0(z) - c)a]^2} = 1. \tag{1.14}$$

The singular solution is then given by the geometrical envelope of the family of curves described by the general solution. It can be found by eliminating the parameter a from the function $k(\theta; a)$ using the condition $\mathrm{d}k/\mathrm{d}a = 0$, which defines the function $a = a(\theta)$ and yields the following singular solution:

$$k(\theta) = a \cos\theta + b(a) \sin\theta, \tag{1.15}$$

https://doi.org/10.1017/jfm.2025.10934 Published online by Cambridge University Press

where

$$\left[a^2 + b(a)^2\right] \int_0^1 \frac{\mathrm{d}z}{[1 - (u_0(z) - c)a]^2} = 1 \quad \text{and} \quad \frac{\mathrm{d}b}{\mathrm{d}a} = -\frac{1}{\tan\theta}. \tag{1.16}$$

There are no parameters in the singular solution, and the associated waves are ring waves (Johnson 1990). We also note that the general solution (1.14) satisfies the equation

$$k'' + k = 0, \tag{1.17}$$

while the singular solution cannot satisfy this equation since it is not a part of the general solution.

The equation derived by Johnson (1990) has the same form as (1.7), but the coefficients are given by rather complicated formulae involving multiple integrals. The new formulation (1.8)–(1.10) allows it to be proved that, for surface ring waves in a homogeneous fluid, the coefficient $\mu_5 = 0$ for any shear flow $u_0(z)$ (Khusnutdinova & Zhang 2016). Indeed, differentiating the generalised Burns condition (1.12) with respect to θ, we obtain

$$2(k + k'') \int_0^1 \frac{k'F + (u_0 - c)(k^2 + k'^2)\sin\theta}{F^3}\,\mathrm{d}z = 0, \tag{1.18}$$

where $k + k'' \neq 0$ on the singular solution, implying that the integral in (1.18) is equal to zero instead. Next, substituting function (1.13) into (1.10), we obtain

$$\mu_5 = -2\rho_0 k\left(k^2 + k'^2\right) \int_0^1 \frac{k'F + (u_0 - c)(k^2 + k'^2)\sin\theta}{F^3}\,\mathrm{d}z, \tag{1.19}$$

implying $\mu_5 = 0$ since the integral in (1.19) is the same as in (1.18). Hence, long surface ring waves in a homogeneous fluid are actually described by a simpler one-dimensional (1-D) cKdV-type equation:

$$\mu_1 A_R + \mu_2 A A_\xi + \mu_3 A_{\xi\xi\xi} + \mu_4 \frac{A}{R} = 0. \tag{1.20}$$

Among some other curious features revealed using the formulation based on the far-field modal decomposition was the qualitatively different behaviour of the wavefronts of surface and interfacial waves propagating over the same flows. For example, the wavefront of the surface ring wave in a two-layer fluid with a piecewise-constant current of increasing strength approaching a critical value was elongated in the direction of the flow, while the wavefront of the interfacial wave was squeezed. This phenomenon was linked to the presence of long-wave instability of plane waves tangent to the ring wave and propagating in the downstream and upstream directions for sufficiently strong currents (see Ovsyannikov 1979; Boonkasame & Milewski 2011; Barros & Choi 2014; Lannes & Ming 2015; Khusnutdinova & Zhang 2016). Similar effects were shown to take place in a two-layer fluid with a two-parameter family of upper-layer currents $u_0 = \gamma((z + d)/d)^\alpha$ for sufficiently small values of α (with $-d$ denoting the position of the interface) by Khusnutdinova (2020), Hooper *et al.* (2021) and in a three-layer fluid for a current with a constant vertical shear (for the second interfacial mode) by Tseluiko *et al.* (2023).

Interestingly, while ring waves associated with the singular solution of the equation for the function $k(\theta)$ (for example, the generalised Burns condition (1.12)) have been studied, waves associated with the general solution were overlooked. Their role in describing plane waves tangent to the ring wave was understood only recently, in connection with the kinematic consideration of hybrid wavefronts on depth-dependent parallel shear flows

https://doi.org/10.1017/jfm.2025.10934 Published online by Cambridge University Press

(Hooper *et al.* 2021), while the related amplitude equation has not been considered at all. One of the aims of the present study is to derive this new amplitude equation

$$\mu_1 A_R + \mu_2 A A_\xi + \mu_3 A_{\xi\xi\xi} + \mu_5 \frac{A_\theta}{R} = 0, \tag{1.21}$$

which we call the KdVθ equation, and understand its role. The overarching aim of the paper, however, is to study the evolution of perturbed nonlinear plane, ring and hybrid waves within the scope of the full 2-D Boussinesq–Peregrine system for surface waves (Peregrine 1967) and to identify features that can be described using the reduced amplitude equations.

In this paper we restrict our numerical considerations to the case of long surface waves in a homogeneous fluid without a shear flow, although all constructions have a counterpart in stratified fluids and with an underlying shear flow, as discussed above. In § 2 we discuss the 2-D Boussinesq–Peregrine system and derive the 2-D counterparts of the approximate conservation laws considered, in the 1-D setting, by Katsaounis, Mitsotakis & Sadaka (2020), Khorbatly & Kalisch (2024) (see Appendix A for details). We also derive a particular version of the KdVθ equation (3.6) directly from this parent system, and include a brief derivation of the known cKdV and Kadomtsev–Petviashvili II (KPII) equations (see, for example, Miles 1978; Ablowitz & Segur 1979; Johnson 1997; Sidorovas *et al.* 2024 and further references therein). The numerical method used to solve the system is discussed in Appendix B.

In § 3 we derive the KdVθ equation (3.3) from the 2-D cKdV-type equation (1.7) for the general setting of a stratified fluid over a parallel shear flow. Then, we show that the KdVθ equation can be mapped to the KdV equation, but the initial condition retains the parametric dependence on the polar angle θ. This allows us to make analytical predictions concerning the 2-D fission of a perturbed line soliton, using the Inverse Scattering Transform (IST, Gardner *et al.* 1967). Long transverse perturbations of line solitons modelled by the KP equation (in particular, the KPII equation, describing water waves) were extensively studied, both from the applied and rigorous perspectives (see Kadomtsev & Petviashvili 1970; Pesenson 1991; Kivshar & Pelinovsky 2000; Mizumachi & Tzvetkov 2012; Mizumachi 2015; Haragus, Li & Pelinovsky 2017; Mizumachi & Shimabukuro 2017; Mizumachi & Shimabukuro 2020 and references therein). However, to the best of our knowledge, the amplitude equation discussed in our paper has not been derived or used before. We show that it can be used instead of the KPII equation to describe the intermediate evolution of sufficiently long perturbations of finite amplitude. The reduction to the KdV equation is discussed in Appendix C.

Next, in §§ 4 and 5 we consider perturbed ring and hybrid waves. Our simulations within the full parent system allow us to investigate the long-time evolution subject to both localised and periodic perturbations. In particular, we find examples illustrating the difference in the behaviour of inward-propagating ring waves depending on the wavelength of the perturbation, which was predicted theoretically by Ostrovskii & Shrira (1976), Shrira & Pesenson (1984), Pesenson (1991). We show that the evolution of the hybrid wave is strongly dependent on whether it is a diverging or converging wave, and that the outward-propagating (diverging) wave is stable. However, the inward-propagating (converging) case leads to a very peculiar instability scenario: there appears a large rogue wave (lump) that disintegrates into several pieces and eventually evolves into a stable 'X-type' structure known from the theory of the KPII equation (e.g. Ablowitz & Curtis 2013; Chakravarty & Kodama 2014; Yuan & Wang 2022). Finally, in § 6 we summarise our results and make remarks about some natural extensions of our present studies.

https://doi.org/10.1017/jfm.2025.10934 Published online by Cambridge University Press

2. The 2-D Boussinesq–Peregrine system and reduced models

We consider surface waves in a homogeneous fluid within the scope of the non-dimensional 2-D Boussinesq–Peregrine system (Peregrine 1967, see also the review Lannes 2020 and references therein for the discussion of asymptotically equivalent systems and rigorous justification), assuming a flat bottom:

$$\eta_t + \nabla \cdot \{(1+\epsilon\eta)\boldsymbol{u}\} = 0, \tag{2.1}$$

$$\boldsymbol{u}_t + \epsilon(\boldsymbol{u}\cdot\nabla)\boldsymbol{u} + \nabla\eta - \frac{\delta^2}{3}\nabla(\nabla\cdot\boldsymbol{u}_t) = \boldsymbol{0}. \tag{2.2}$$

Here $\boldsymbol{u} = (u, v)^{\mathrm{T}}$ are the depth-averaged horizontal velocities, η is the free-surface elevation, ϵ is the small-amplitude parameter and δ is the long-wavelength parameter.

The 2-D Boussinesq–Peregrine system conserves mass exactly, while momentum and energy are conserved asymptotically (the details of our calculations can be found in Appendix A). The integral forms for these conservation laws can be written as

$$\frac{\mathrm{d}\mathcal{M}}{\mathrm{d}t} = \frac{\mathrm{d}}{\mathrm{d}t}\iint_D \eta \,\mathrm{d}x\mathrm{d}y = 0, \tag{2.3}$$

$$\frac{\mathrm{d}\mathcal{P}}{\mathrm{d}t} = \frac{\mathrm{d}}{\mathrm{d}t}\iint_D (1+\epsilon\eta)\,\boldsymbol{u}\,\mathrm{d}x\mathrm{d}y = O(\epsilon^2, \epsilon\delta^2, \delta^4), \tag{2.4}$$

$$\frac{\mathrm{d}\mathcal{E}}{\mathrm{d}t} = \frac{\mathrm{d}}{\mathrm{d}t}\iint_D \frac{1}{2}\left(|\boldsymbol{u}|^2 + \eta^2\right)\,\mathrm{d}x\mathrm{d}y = O(\epsilon, \delta^2), \tag{2.5}$$

respectively, where $D = \{(x, y)|x_1 \leqslant x \leqslant x_2,\, y_1 \leqslant y \leqslant y_2\}$ is the doubly periodic rectangular computational domain. These results generalise the 1-D results obtained by Katsaounis *et al.* (2020), Khorbatly & Kalisch (2024). In order to match the derivation of the reduced amplitude equations we choose the balance $\epsilon = \delta^2$. We therefore expect mass to be conserved in numerical simulations to machine precision, while the deviations in momentum and energy should scale as ϵ^2 and ϵ, respectively. This was indeed the case in our simulations (see the discussion in Appendix A). We numerically solve the system (2.1) and (2.2) using the pseudospectral method outlined in Appendix B.

Next, we derive the KdVθ and cKdV equations directly from the system (2.1) and (2.2), in the slow radius form. We apply the non-axisymmetric change of variables $(t, x, y) \to (t, r, \theta)$ to give

$$\eta_t + U_r + \frac{U}{r} + \frac{V_\theta}{r} + \epsilon\left[U\eta_r + \eta U_r + \frac{U\eta + V\eta_\theta + \eta V_\theta}{r}\right] = 0, \tag{2.6}$$

$$U_t + \eta_r + \frac{\epsilon}{3}\left[\frac{U_t + V_{t\theta}}{r^2} - \frac{U_{rt} - 3VU_\theta + 3V^2 - V_{rt\theta}}{r} - U_{rrt} + 3UU_r\right] = 0, \tag{2.7}$$

$$V_t + \frac{\eta_\theta}{r} + \frac{\epsilon}{3}\left[-\frac{U_{t\theta} + V_{t\theta\theta}}{r^2} - \frac{3UV + 3VV_\theta - U_{tr\theta}}{r} + 3UV_r\right] = 0, \tag{2.8}$$

where the variables U and V are the cylindrically projected velocity components of $\boldsymbol{u}$:

$$u = U\cos\theta - V\sin\theta, \quad v = U\sin\theta + V\cos\theta. \tag{2.9}$$

To leading order, we obtain

$$\eta_{tt} - \eta_{rr} - \frac{\eta_r}{r} - \frac{\eta_{\theta\theta}}{r^2} = 0, \tag{2.10}$$

$$U_t + \eta_r = 0, \tag{2.11}$$

$$V_t + \frac{\eta_\theta}{r} = 0, \tag{2.12}$$

https://doi.org/10.1017/jfm.2025.10934 Published online by Cambridge University Press

where $\eta = \eta(\xi)$, given $\xi = rk(\theta) - t$, is an exact solution of (2.10) if $k(\theta)$ has the form $k(\theta) = a\cos\theta + b(a)\sin\theta$ and $a^2 + b(a)^2 = 1$ (coinciding with the general solution (1.14) for $u_0(z) = 0$), e.g. $a = \cos\varphi$ and $b = \sin\varphi$, where φ then has the meaning of the angle between the normal to the wavefront and the positive x direction. In particular, if $\varphi = 0$, i.e. waves propagate in the x direction, then $\xi = r\cos\theta - t = x - t$.

We then consider solutions in the far field such that $R = \epsilon rk(\theta) \sim O(1)$ and apply the change of variables $(t, r, \theta) \to (R, \xi, \theta)$ to obtain

$$\eta_\xi - kU_\xi - k'V_\xi - \epsilon\left[kU_R + k\frac{U}{R} + k'V_R + k\frac{V_\theta}{R} + k(U\eta)_\xi + k'(V\eta)_\xi\right] = O(\epsilon^2), \quad (2.13)$$

$$U_\xi - k\eta_\xi - \frac{\epsilon}{3}\left[3k\eta_R + 3k'VU_\xi + kk'V_{\xi\xi\xi} + k^2U_{\xi\xi\xi} + 3kUU_\xi\right] = O(\epsilon^2), \quad (2.14)$$

$$V_\xi - k'\eta_\xi - \frac{\epsilon}{3}\left[3k'\eta_R + 3k\frac{\eta_\theta}{R} + 3k'VV_\xi + kk'U_{\xi\xi\xi} + 3kUV_\xi - k'^2V_{\xi\xi\xi}\right] = O(\epsilon^2). \quad (2.15)$$

We seek a solution of (2.13)–(2.15) in the form of an asymptotic multiple-scale expansion

$$\eta(R, \xi, \theta) = \eta^{(0)}(R, \xi, \theta) + \epsilon\eta^{(1)}(R, \xi, \theta) + O(\epsilon^2) \quad \text{as} \quad \epsilon \to 0, \quad (2.16)$$

and similarly for U and V. At leading order, $O(1)$, we obtain

$$\eta^{(0)} = \eta^{(0)}(R, \xi, \theta), \quad (2.17)$$

$$U^{(0)} = k\eta^{(0)}, \quad (2.18)$$

$$V^{(0)} = k'\eta^{(0)}, \quad (2.19)$$

assuming that any disturbances are generated only by the propagating waves. At next order, $O(\epsilon)$, we obtain

$$\eta^{(1)}_\xi - kU^{(1)}_\xi - k'V^{(1)}_\xi = kU^{(0)}_R + k\frac{U^{(0)}}{R} + k'V^{(0)}_R + k\frac{V^{(0)}_\theta}{R} + k(U^{(0)}\eta^{(0)})_\xi + k'(V^{(0)}\eta^{(0)})_\xi, \quad (2.20)$$

$$U^{(1)}_\xi = k\eta^{(1)}_\xi + k\eta^{(0)}_R + k'V^{(0)}U^{(0)}_\xi + \frac{1}{3}kk'V^{(0)}_{\xi\xi\xi} + \frac{1}{3}k^2U^{(0)}_{\xi\xi\xi} + kU^{(0)}U^{(0)}_\xi, \quad (2.21)$$

$$V^{(1)}_\xi = k'\eta^{(1)}_\xi + k'\eta^{(0)}_R + k\frac{\eta^{(0)}_\theta}{R} + k'V^{(0)}V^{(0)}_\xi + \frac{1}{3}kk'U^{(0)}_{\xi\xi\xi} + k'^2V^{(0)}_{\xi\xi\xi} + kU^{(0)}V^{(0)}_\xi, \quad (2.22)$$

from which substituting (2.18) and (2.19), and (2.21) and (2.22) into (2.20), to eliminate $\eta^{(1)}$, $U^{(0)}$, $U^{(1)}$, $V^{(0)}$ and $V^{(1)}$, gives the KdVθ equation for perturbed surface plane waves propagating at an angle φ to the positive x direction as

$$2\eta^{(0)}_R + 3\eta^{(0)}\eta^{(0)}_\xi + \frac{1}{3}\eta^{(0)}_{\xi\xi\xi} + 2kk'\frac{\eta^{(0)}_\theta}{R} = 0. \quad (2.23)$$

The corresponding leading-order Cartesian velocities are calculated from (2.9) and (2.18), (2.19) to be

$$u^{(0)} = \cos\varphi\,\eta^{(0)} \qquad \text{and} \qquad v^{(0)} = \sin\varphi\,\eta^{(0)}. \quad (2.24)$$

https://doi.org/10.1017/jfm.2025.10934 Published online by Cambridge University Press

If x is chosen to be the direction of propagation then $\varphi = 0$, $k = \cos\theta$, and (2.23) takes the form

$$2\eta^{(0)}_R + 3\eta^{(0)}\eta^{(0)}_\xi + \frac{1}{3}\eta^{(0)}_{\xi\xi\xi} - 2\sin\theta\cos\theta\frac{\eta^{(0)}_\theta}{R} = 0, \tag{2.25}$$

where $R = \epsilon x$, $\xi = x - t$ and the corresponding Cartesian velocities are $u^{(0)} = \eta^{(0)}$ and $v^{(0)} = 0$. This is a particular form of the KdVθ equation (3.3), derived directly from the 2-D Boussinesq–Peregrine system (2.1) and (2.2).

The cKdV equation can be derived using a simpler asymptotic expansion (see, for example, Miles 1978; Johnson 1997; Sidorovas *et al.* 2024 and references therein). We apply the axisymmetric change of variables $(t, x, y) \to (t, r)$ to (2.1) and (2.2), which yields

$$\eta_t + U_r + \frac{U}{r} + \epsilon\left[U\eta_r + \eta U_r + \frac{U\eta}{r}\right] = 0, \tag{2.26}$$

$$U_t + \eta_r + \frac{\epsilon}{3}\left[\frac{U_t}{r^2} - \frac{U_{rt}}{r} - U_{rrt} + 3UU_r\right] = 0, \tag{2.27}$$

where U is the radial cylindrical velocity component of $\boldsymbol{u}$. To leading order, we therefore obtain

$$\eta_{tt} - \eta_{rr} - \frac{\eta_r}{r} = 0, \tag{2.28}$$

$$u_t + \eta_r = 0, \tag{2.29}$$

where $\eta = \eta(\xi)$, given $\xi = r - t$, is an exact solution of (2.28). We then perform the change of variables $(t, r) \to (R, \xi)$, where $R = \epsilon r$ is the slow radius variable and $\xi = r - t$ is the fast spatial variable in a moving coordinate frame, giving

$$\eta_\xi - U_\xi - \epsilon\left[U_R + \frac{U}{R} + U\eta_\xi + \eta U_\xi\right] = O(\epsilon^2), \tag{2.30}$$

$$U_\xi - \eta_\xi - \frac{\epsilon}{3}\left[3\eta_R + 3UU_\xi + U_{\xi\xi\xi}\right] = O(\epsilon^2). \tag{2.31}$$

We now seek a solution of (2.30) and (2.31) in the form

$$\eta(R, \xi) = \eta^{(0)}(R, \xi) + \epsilon\eta^{(1)}(R, \xi) + O(\epsilon^2) \quad \text{as} \quad \epsilon \to 0, \tag{2.32}$$

and similarly for the variable U. We then consider solutions in the far field such that $R \sim O(1)$, which to leading order yields

$$\eta^{(0)}_\xi - U^{(0)}_\xi = 0, \tag{2.33}$$

giving that $U^{(0)} = \eta^{(0)}$, assuming that any disturbances are generated only by the propagating waves. At next order, we find that

$$\eta^{(1)}_\xi - U^{(1)}_\xi = U^{(0)}_R + \frac{U^{(0)}}{R} + 2\eta^{(0)}\eta^{(0)}_\xi, \tag{2.34}$$

$$U^{(1)}_\xi = \eta^{(1)}_\xi + \eta^{(0)}_R + U^{(0)}U^{(0)}_\xi + \frac{1}{3}U^{(0)}_{\xi\xi\xi}, \tag{2.35}$$

which after substituting (2.33) and (2.35) into (2.34) gives the axisymmetric cKdV equation for surface waves as

$$2\eta^{(0)}_R + 3\eta^{(0)}\eta^{(0)}_\xi + \frac{1}{3}\eta^{(0)}_{\xi\xi\xi} + \frac{\eta^{(0)}}{R} = 0. \tag{2.36}$$

https://doi.org/10.1017/jfm.2025.10934 Published online by Cambridge University Press

Recalling that the depth-averaged Cartesian velocities are given by a linear combination of the polar velocity projections U and V by (2.9), this gives the Cartesian velocity components

$$u^{(0)} = \frac{x}{\sqrt{x^2+y^2}}\,\eta^{(0)}, \quad v^{(0)} = \frac{y}{\sqrt{x^2+y^2}}\,\eta^{(0)}. \tag{2.37}$$

Finally, the KPII equation is derived using the change of variables $(t, x, y) \to (T, \xi, Y)$, where $T = \epsilon t$, $\xi = x - t$ and $Y = \sqrt{\epsilon}y$ (see, for example, Ablowitz & Segur 1979; Johnson 1997 and references therein). We also scale the Cartesian velocity in the y direction as $v \to \sqrt{\epsilon}v$ to remain consistent with the coordinate scaling. Applying this change of variables to (2.1) and (2.2) gives

$$u_\xi - \eta_\xi + \epsilon\left(v_Y + \eta u_\xi + u\eta_\xi + \eta_T\right) = O(\epsilon^2), \tag{2.38}$$

$$\eta_\xi - u_\xi + \epsilon\left(uu_\xi + \frac{1}{3}u_{\xi\xi\xi} + u_T\right) = O(\epsilon^2), \tag{2.39}$$

$$\eta_Y - v_\xi + \epsilon\left(uv_\xi + \frac{1}{3}u_{\xi\xi Y} + v_T\right) = O(\epsilon^2). \tag{2.40}$$

We now seek a solution of (2.38)–(2.40) in the form

$$\eta(T,\xi,Y) = \eta^{(0)}(T,\xi,Y) + \epsilon\eta^{(1)}(T,\xi,Y) + O(\epsilon^2) \quad \text{as} \quad \epsilon \to 0, \tag{2.41}$$

and similarly for the variables u and v. We then consider solutions in the far field such that $T \sim O(1)$, and to leading order, $O(1)$, we obtain

$$u^{(0)}_\xi = \eta^{(0)}_\xi, \tag{2.42}$$

$$v^{(0)}_\xi = \eta^{(0)}_Y, \tag{2.43}$$

such that $u^{(0)} = \eta^{(0)}$, assuming that any disturbances are generated only by the propagating waves. At the following order, $O(\epsilon)$, we obtain

$$\eta^{(1)}_\xi - u^{(1)}_\xi = v^{(0)}_Y + \eta^{(0)}u^{(0)}_\xi + u^{(0)}\eta^{(0)}_\xi + \eta^{(0)}_T, \tag{2.44}$$

$$u^{(1)}_\xi - \eta^{(1)}_\xi = u^{(0)}u^{(0)}_\xi + \frac{1}{3}u^{(0)}_{\xi\xi\xi} + u^{(0)}_T, \tag{2.45}$$

from which, taking the sum of (2.44) and (2.45) and substituting (2.42) gives

$$2\eta^{(0)}_T + 3\eta^{(0)}\eta^{(0)}_\xi + \frac{1}{3}\eta^{(0)}_{\xi\xi\xi} + v^{(0)}_Y = 0. \tag{2.46}$$

Taking the ξ derivative of (2.46) and substituting the Y derivative of (2.43) gives the KPII equation for surface waves:

$$\left(2\eta^{(0)}_T + 3\eta^{(0)}\eta^{(0)}_\xi + \frac{1}{3}\eta^{(0)}_{\xi\xi\xi}\right)_\xi + \eta^{(0)}_{YY} = 0. \tag{2.47}$$

The slow time variable T is more commonly used for the KPII equation and in the later sections makes comparisons to the solutions of the 2-D Boussinesq–Peregrine equations simpler. For the KdVθ and cKdV equations, the R-variable version could be more natural (see, for example, the discussion concerning the cKdV equation in Sidorovas *et al.* 2024), but the slow time $T = \epsilon t$ version is easily recovered by the change of variables $(R, \xi, \theta) \to (T, \xi, \theta)$.

https://doi.org/10.1017/jfm.2025.10934 Published online by Cambridge University Press

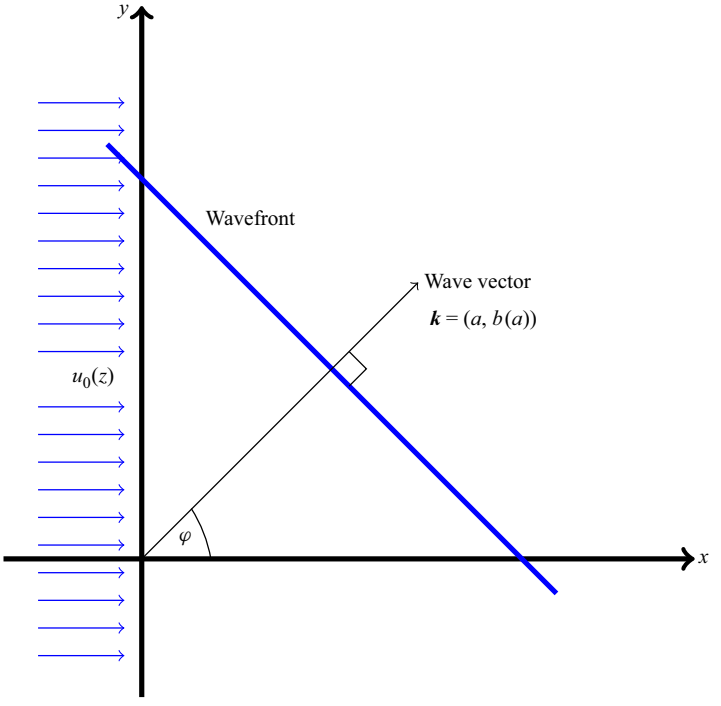


Figure 2. Wavefront and wave vector of a plane wave propagating at an angle φ to the direction of the shear flow $u_0(z)$.

3. The KdVθ equation and perturbed plane waves

In this section we first derive the KdVθ equation from the $(2+1)$-dimensional amplitude equation (1.7) for a stratified fluid with a parallel shear flow, which was previously derived from the full set of Euler equations with the free-surface and flat-bottom boundary conditions by Khusnutdinova & Zhang (2016). Since the general solution of the equation for the function k is associated with plane waves (Hooper *et al.* 2021), assuming that the waves exist, it will be in the form

$$k(\theta; a) = a\cos\theta + b(a)\sin\theta, \tag{3.1}$$

with a problem-specific relation $b = b(a)$. Indeed, the waves associated with the general solution (3.1) have the fast variable

$$\xi = rk(\theta) - st = ax + b(a)y - st, \tag{3.2}$$

with the constants a and $b(a)$ having the meaning of the two wavenumbers of the plane wave propagating at an angle $\tan\varphi = b(a)/a$ to the flow (see figure 2). The wavefronts are tangent to the ring wave associated with the corresponding singular solution, obtained as a geometrical envelope of the general solution (see figure 3 for $u_0(z) = \gamma z$, $\gamma = \text{const}$).

Next, on the general solution (3.1), we obtain $k^2 + k'^2 = a^2 + b(a)^2$ and $F = -s + [u_0(z) - c]a$. Hence, the modal equations (1.3)–(1.5) become θ independent, and therefore, the modal function is also θ independent, i.e. $\phi = \phi(z)$. It then implies, using (1.9) and (1.17), that $\mu_4 = 0$ for any stratification and any parallel shear flow $u_0(z)$.

https://doi.org/10.1017/jfm.2025.10934 Published online by Cambridge University Press

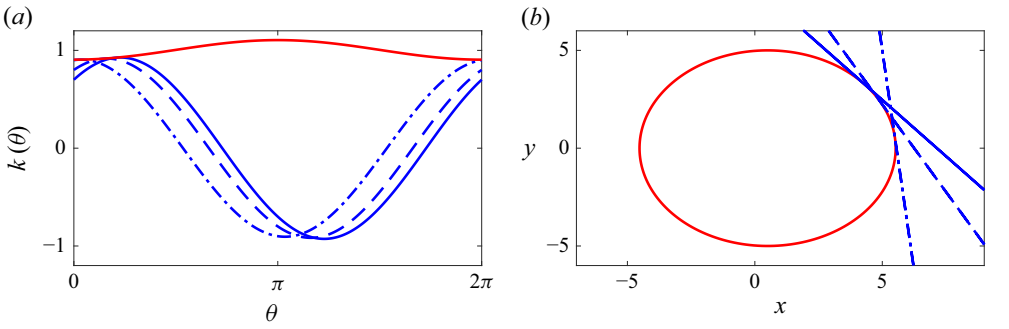


Figure 3. (*a*) The general solution (1.14) for $a = 0.7$ (blue), $a = 0.8$ (dashed blue) and $a = 0.9$ (dashed dot blue) and its envelope (the singular solution, solid red) all for $u_0(z) = \gamma z$, $\gamma = 0.2$. (*b*) The wavefronts corresponding to the general and singular solutions from (*a*) described by $rk(\theta) = 5$.

Hence, we obtain the amplitude equation, which has the form

$$\mu_1 A_R + \mu_2 A A_\xi + \mu_3 A_{\xi\xi\xi} + \mu_5 \frac{A_\theta}{R} = 0, \tag{3.3}$$

and the coefficients of this equation are computed using the general solution (3.1) in (1.8) and (1.10). Generally, the coefficient μ_5 has a non-trivial dependence on θ, while μ_1, μ_2, μ_3 are some constants. For example, for surface waves in a homogeneous fluid over the linear shear flow $u_0(z) = \gamma z$ with $\gamma = \text{const}$, we obtain

$$\mu_1 = \frac{2s - \gamma a}{s(s - \gamma a)^2}, \quad \mu_2 = \frac{[a^2 + b(a)^2]^2(3s - 3s\gamma a + \gamma^2 a^2)}{s^3(s - \gamma a)^3}, \quad \mu_3 = \frac{[a^2 + b(a)^2]^2}{3s^2}, \tag{3.4}$$

$$\mu_5 = \frac{[a\cos\theta + b(a)\sin\theta][2b(a)(s - \gamma a)\cos\theta - (2as + a^2\gamma - b(a)^2\gamma)\sin\theta]}{s(s - \gamma a)^2}. \tag{3.5}$$

When there is no shear flow, the coefficients reduce to $\mu_1 = 2$, $\mu_2 = 3$, $\mu_3 = 1/3$ and $\mu_5 = -2\sin\theta\cos\theta$, resulting in the equation

$$A_R + \frac{3}{2} A A_\xi + \frac{1}{6} A_{\xi\xi\xi} - \frac{1}{2}\sin 2\theta \frac{A_\theta}{R} = 0, \tag{3.6}$$

which coincides with (2.25) derived in § 2 directly from the 2-D Boussinesq–Peregrine system. If the wave has a plane wavefront then $A_\theta = 0$ (there is no change in the tangential direction along the wavefront), and the amplitude (3.3) (and hence (3.6)) has a reduction to the KdV equation (see Appendix C). However, the full equation (3.3), and its particular case (3.6), are more general. To the best of our knowledge, (3.3) and (3.6) have not been derived before and we will refer to both as the KdVθ equation.

In this section we consider plane waves subject to long transverse perturbations. As an example, we apply long transverse amplitude perturbations of finite strength to the line-soliton solution of the KdVθ equation (3.6), where we have changed the variables from (R, ξ, θ) to $(T = \epsilon t, \xi, \theta)$ for a more accurate comparison of numerical solutions of the reduced amplitude equation to those of the 2-D Boussinesq–Peregrine system. To leading order, the change of variable $R \to T$ does not change the form of the amplitude equation (3.3), provided we map $\mu_1 \to \mu_1/s$ and $\mu_5 \to \mu_5/s$:

$$\mu_1 A_T + s\mu_2 A A_\xi + s\mu_3 A_{\xi\xi\xi} + \mu_5 \frac{A_\theta}{T} = 0. \tag{3.7}$$

https://doi.org/10.1017/jfm.2025.10934 Published online by Cambridge University Press

The KdVθ equation (3.7) can be analysed analytically, using a mapping similar to that noted by Johnson (1990) for ring waves. Indeed, for every value of θ, the change of variables

$$\tilde{\theta} = T \exp\left(-\int \frac{\mu_1}{\mu_5}\,\mathrm{d}\theta\right) \tag{3.8}$$

maps the KdVθ equation (3.7) to the usual KdV equation

$$A_T + \frac{s\mu_2}{\mu_1} A A_\xi + \frac{s\mu_3}{\mu_1} A_{\xi\xi\xi} = 0, \tag{3.9}$$

since (1.8) and (1.10) imply that the only θ-dependent coefficient in (3.7), and the slow R version (3.3), is μ_5. However, the initial condition for the KdV equation (3.9) will have parametric dependence on $\tilde{\theta}$, and hence, on the polar angle θ.

Here, we consider surface waves without a shear flow. Then $s = 1$, and the KdVθ equation (3.7), for the waves propagating in the x direction, takes the form

$$A_T + \frac{3}{2} A A_\xi + \frac{1}{6} A_{\xi\xi\xi} - \frac{1}{2} \sin 2\theta \frac{A_\theta}{T} = 0, \tag{3.10}$$

where

$$T = \epsilon t, \quad \xi = x - t, \quad \theta = \arctan\frac{y}{x}. \tag{3.11}$$

A long transverse amplitude perturbation is added to the initial condition, at some $T = T_0$, by multiplying the initial condition by a suitable function of θ. The unperturbed initial condition is the θ-independent exact line-soliton solution of the KdVθ equation (3.10), given by

$$A_0(T_0, \xi, \theta) = 2\tilde{v}\,\mathrm{sech}^2\left(\frac{1}{2}\sqrt{6\tilde{v}}\left[\xi - \tilde{v}T_0 - \xi_0\right]\right), \tag{3.12}$$

where $\tilde{v} > 0$ and ξ_0 are some constants. We take the perturbed initial condition to be in the form

$$A(T_0, \xi, \theta) = \left(1 + \alpha\,\mathrm{sech}^2\,\beta\theta\right) A_0(T_0, \xi, \theta), \tag{3.13}$$

although we could choose to multiply by any other function of θ. Here, the constants α and β control the amplitude and width of the perturbation, $\tilde{v}$ is the speed of the soliton and ξ_0 is an initial phase shift. The multiplication of the original sech^2 soliton by this θ-dependent function generates a smooth, localised perturbation in the central region of the wavefront.

The mapping (3.8) yields

$$\tilde{\theta} = T \tan\theta, \tag{3.14}$$

and the KdV equation (3.9) simplifies to become

$$A_T + \frac{3}{2} A A_\xi + \frac{1}{6} A_{\xi\xi\xi} = 0, \tag{3.15}$$

which we now need to solve for the initial condition

$$A(T_0, \xi, \tilde{\theta}) = \left[1 + \alpha\,\mathrm{sech}^2\left(\beta \arctan\frac{\tilde{\theta}}{T_0}\right)\right] A_0\left(T_0, \xi, \arctan\frac{\tilde{\theta}}{T_0}\right). \tag{3.16}$$

https://doi.org/10.1017/jfm.2025.10934 Published online by Cambridge University Press

Next, to use the results of the IST (see Gardner *et al.* 1967), we cast the KdV equation (3.15) into the canonical form

$$U_\tau - 6UU_X + U_{XXX} = 0, \tag{3.17}$$

via the scalings $U = -3A/2$, $\tau = T/6$, $X = \xi$. The wavefield is then defined by the spectrum of the Schrödinger equation

$$\Psi_{XX} + \left[\lambda - U(\tau_0, X; \tilde{\theta})\right]\Psi = 0, \tag{3.18}$$

where the potential is given by the perturbed initial condition (3.13), i.e.

$$U(\tau_0, X; \tilde{\theta}) = -\Lambda \operatorname{sech}^2\left(\frac{X - 6\tilde{v}\tau_0 - \xi_0}{L}\right), \tag{3.19}$$

where

$$\Lambda = 3\tilde{v}\Delta, \quad L = \frac{2}{\sqrt{6\tilde{v}}}, \quad \Delta(\tau_0; \tilde{\theta}) = 1 + \alpha \operatorname{sech}^2\left(\beta \arctan\frac{\tilde{\theta}}{6\tau_0}\right), \tag{3.20}$$

i.e. we have different initial conditions for different values of $\tilde{\theta}$ and, hence, for different values of the polar angle θ. The number of generated solitons depends on θ and is given by the greatest integer satisfying the inequality

$$N(\tau_0; \tilde{\theta}) < \frac{1}{2}\left[\left(1 + 4\Lambda L^2\right)^{\frac{1}{2}} + 1\right] \tag{3.21}$$

(see, e.g., Landau & Lifshitz (1959)). The discrete eigenvalues are given by

$$\lambda = -k_n^2, \tag{3.22}$$

where

$$k_n(\tau_0; \tilde{\theta}) = \frac{1}{2L}\left[\left(1 + 4\Lambda L^2\right)^{\frac{1}{2}} - (2n-1)\right] > 0, \quad n = 1, 2, \ldots, N. \tag{3.23}$$

For positive α and $\tilde{v}$ values, the central perturbed region fissions into at least two solitons and a dispersive wave train. However, for small α values, the secondary soliton is small and for a very long time it blends with the radiation. The outer, unperturbed section of the line soliton propagates as a single curved soliton. We therefore expect a localised 2-D region of radiation behind a smaller soliton in the wake of the main perturbed soliton. The long-time asymptotics takes the form

$$U(\tau, X; \tilde{\theta}) \simeq -\sum_{n=1}^{N} 2k_n^2 \operatorname{sech}^2\left(k_n(X - 4k_n^2\tau - X_n)\right) + \text{radiation} \tag{3.24}$$

(e.g. Drazin 1983), where the phase shifts are given by

$$X_1 = \frac{1}{2k_1}\ln\left(\frac{c_1}{2k_1}\right), \quad X_n = \frac{1}{2k_n}\ln\left(\frac{c_n}{2k_n}\prod_{m=1}^{n-1}\left(\frac{k_n - k_m}{k_n + k_m}\right)^2\right), \quad n > 1, \tag{3.25}$$

and the constants c_n are found as

$$c_n = \left(\int_{-\infty}^{\infty} \Psi_n^2(x)\,\mathrm{d}x\right)^{-1}, \tag{3.26}$$

https://doi.org/10.1017/jfm.2025.10934 Published online by Cambridge University Press

where $\Psi_n(X)$ is the eigenfunction of (3.18) corresponding to the nth eigenvalue, $-k_n^2$:

$$\Psi_n = \text{const}\left(1-\tanh^2\frac{x}{L}\right)^{\frac{k_nL}{2}}\ {}_2F_1\left(1-n, 2k_nL+n, k_nL+1, \frac{1-\tanh\frac{x}{L}}{2}\right). \quad (3.27)$$

Here, ${}_2F_1(\cdot)$ is the hypergeometric function and the constant should be chosen to normalise the eigenfunction at infinity:

$$\Psi_n \sim \exp^{-k_nx} \quad \text{as} \quad x\to+\infty. \quad (3.28)$$

We can therefore analytically describe the main soliton and the extra solitons produced for every direction defined by the polar angle θ.

When there is no perturbation, i.e. $\Delta = 1$, the solution is simply the exact line-soliton solution. When $\Delta > 1$, there is a localised perturbation to the wavefront, detectable in some region given by $-\tilde{\theta}_1 \lesssim \tilde{\theta} \lesssim \tilde{\theta}_1$ such that the amplitude $A(T,\xi,\theta) \gtrsim A(T_0,\xi,\theta)+\epsilon$. The estimate for the region determining where the perturbation lies is therefore given by the formula $4k_1(\tilde{\theta})^2/3 \gtrsim -2U(\tau_0, X;\tilde{\theta})/3+\epsilon$ arising from (3.24). The small secondary solitons are then detectable when $A(T,\xi,\theta)\gtrsim\epsilon$ and, hence, when $4k_n(\tilde{\theta})^2/3\gtrsim\epsilon$. These regions are shown in figure 4, where we compare the performance of the KdVθ equation with the results of direct numerical simulations for the parent system.

The corresponding initial condition in the xy plane for the 2-D Boussinesq–Peregrine system (2.1) and (2.2) is obtained using the initial condition to the KdVθ equation (3.13):

$$\eta(t_0,x,y) = 2\tilde{v}\left(1+\alpha\,\text{sech}^2\left(\beta\arctan\frac{y}{x}\right)\right)\text{sech}^2\left(\frac{1}{2}\sqrt{6\tilde{v}}\,(x-(1+\epsilon\tilde{v})t_0-\xi_0)\right), \quad (3.29)$$

$$u(t_0,x,y)=\eta(t_0,x,y), \quad v(t_0,x,y)=0. \quad (3.30)$$

Here $\xi_0 = \text{const}$. The computation parameters can be found in table 1 and the corresponding numerical results are shown in figure 4.

We solve the 2-D Boussinesq–Peregrine system for $t\in[20,120]$ and $\epsilon = 0.05$, where comparison is made to the KdVθ equation that is solved for $T\in[1,6]$. Comparisons can therefore be made at the same time. There is good quantitative agreement between the two solutions around the slow time value $T = 2$. The second soliton is emerging and there is also some extra radiation in the 2-D Boussinesq–Peregrine system. In longer runs, shown for the slow time value $T = 6$, the agreement between the KdVθ equation and the 2-D Boussinesq–Peregrine equations worsens. The main perturbed soliton starts to split sideways, spreading out across the wavefront and in doing so reduces in amplitude in the centre. This feature is not seen in the KdVθ equation. The second soliton has now fissioned from the original soliton, and the analytical estimates based on the IST give good predictions for the perturbed regions of the main and secondary solitons. In the 2-D Boussinesq–Peregrine equations the second soliton has radiated more than in the KdVθ regime, leading to the noticeable difference. However, there is still good qualitative agreement between the full parent system and the reduced model, despite the strong perturbation and long propagation time.

Eventually, all strong, long transverse amplitude perturbations split and travel sideways along the wavefront with two ring-wave arcs being radiated as the perturbation travels bidirectionally along the wavefront. For long enough perturbations, the L^∞ norm $||d||_\infty$ equal to the maximum absolute value of the difference between solutions of the 2-D Boussinesq–Peregrine system and the KdVθ equation is consistent with the model

https://doi.org/10.1017/jfm.2025.10934 Published online by Cambridge University Press

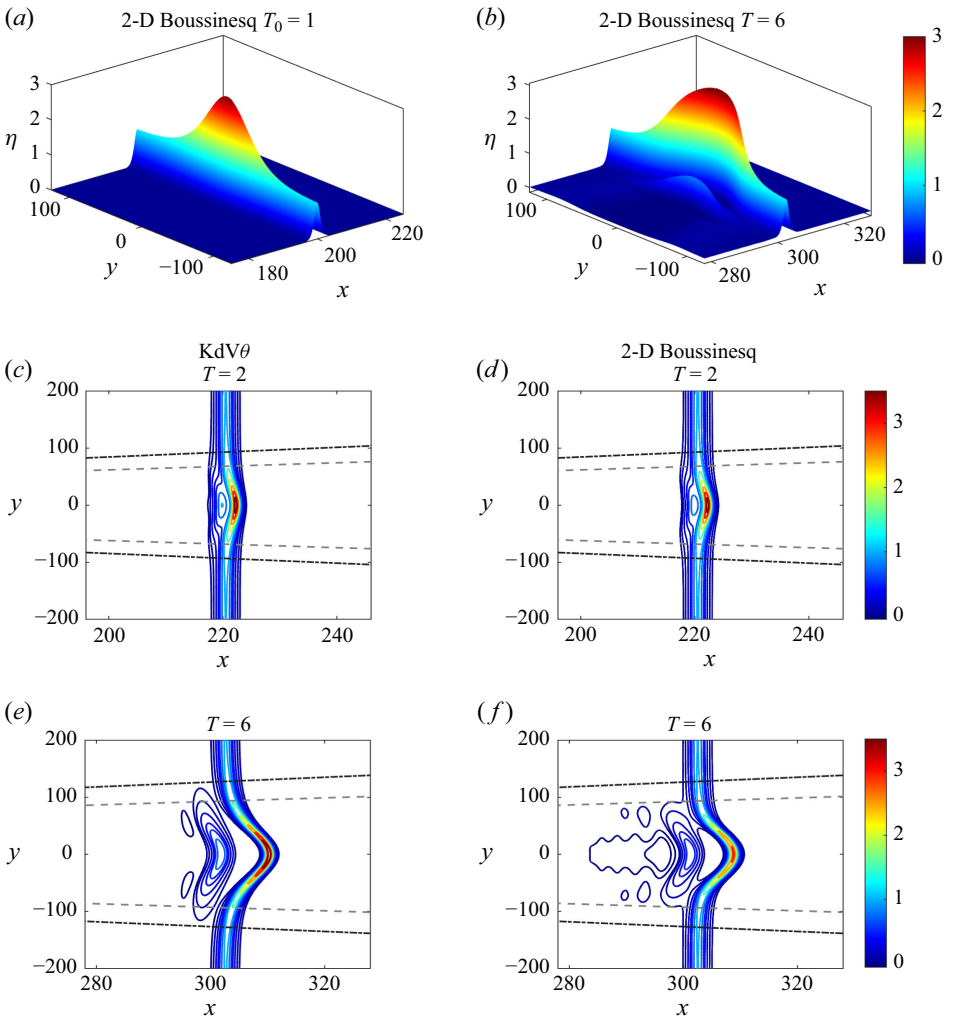


Figure 4. Two-dimensional (*a*,*b*) and contour (*c*,*d*,*e*,*f*) plots of the numerical solution of both the 2-D Boussinesq–Peregrine system (*a*,*b*,*d*,*f*) and the KdVθ equation (*c*,*e*) for a perturbed line soliton, where $\alpha = 2$, $\beta = 5$, $\tilde{v} = 0.5$, $\xi_0 = 180$, $\epsilon = 0.05$ and $T \in [1, 6]$. The dark grey (dash-dotted) and the light grey (dashed) lines illustrate theoretical (IST) predictions for the perturbed regions of the main and secondary solitons, respectively.

and scales as $O(\epsilon)$. The computation parameters in table 2 correspond to figure 5. In figure 5, for the strong perturbation of $\alpha = 0.5$ considered here and the perturbation width parameter $\beta = 20$, the fitted line has the gradient 0.76. When the perturbation is wider, $\beta = 10$, the fitted line has a greater gradient of 1.1. Therefore, for sufficiently long perturbations, the KdVθ equation is accurate to $O(\epsilon)$. We note that the KPII equation is valid too in this regime, as well as for narrower perturbations. However, the KdVθ equation is a much simpler model, which can be used to describe the intermediate asymptotics of plane waves subject to sufficiently long transverse perturbations of finite amplitude.

4. Perturbed ring waves

In this section we extend the studies of concentric ring waves by Chwang & Wu (1977), Sidorovas *et al.* (2024) to non-axisymmetric perturbed ring waves, within the framework

https://doi.org/10.1017/jfm.2025.10934 Published online by Cambridge University Press

Regime	$x \times y$	N_x	N_y	Δ_t
Boussinesq	$[150, 400] \times [-250, 250]$	2500	4000	10^{-2}
Regime	$\xi \times \theta$	N_ξ	N_θ	Δ_T
KdVθ	$[0, 200] \times [-\pi/4, \pi/4]$	2000	500	5×10^{-4}

Table 1. Computation parameters for the KdVθ equation and 2-D Boussinesq–Peregrine system to generate figure 4.

Regime	$x \times y$	N_x	N_y	Δ_t
Boussinesq	$[140, 280] \times [-125, 125]$	1400	2500	10^{-2}
Regime	$\xi \times \theta$	N_ξ	N_θ	Δ_T
KdVθ	$[100, 300] \times [-\pi/4, \pi/4]$	2000	500	5×10^{-4}

Table 2. Computation parameters for the KdVθ equation and 2-D Boussinesq–Peregrine system to generate figure 5.

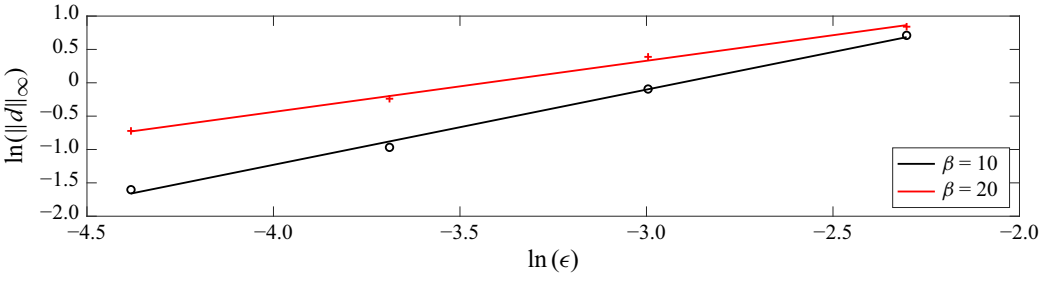


Figure 5. Convergence of the solution of the KdVθ equation to the solution of the 2-D Boussinesq–Peregrine system for different values of parameter β of the transverse perturbation and small parameter ϵ, where $||d||_\infty$ is the L^∞ norm of the difference between solutions of the 2-D Boussinesq–Peregrine system and KdVθ equation, where $\alpha = 0.5$, $\tilde{v} = 0.5$, $\xi_0 = 200$ and $T \in [1, 2]$.

of the 2-D Boussinesq–Peregrine system (2.1) and (2.2). We use the cKdV equation (2.36) and the related formulae (2.37) for velocity components to define the initial conditions for our numerical runs, and consider both localised and periodic perturbations of concentric waves.

We consider a ring wave that is placed sufficiently far away from the origin. Then, the cylindrical divergence/convergence term in the cKdV equation (2.36) can be treated as a perturbation of the KdV equation, and one can consider the axisymmetric solution initiated by the KdV soliton bent into a ring wave (see Ko & Kuel 1979; Dorfman, Pelinovsky & Stepanyants 1981; Johnson 1999; Sidorovas *et al.* 2024):

$$\eta(t_0, x, y) = 2\tilde{v}\,\mathrm{sech}^2\left(\frac{1}{2}\sqrt{6\tilde{v}}\left[\sqrt{x^2+y^2} - (1+\epsilon\tilde{v})t_0 - r_0\right]\right). \tag{4.1}$$

Here, $\tilde{v} > 0$ and r_0 are some constants. The Cartesian velocities u and v are defined using the related approximations given by (2.37).

https://doi.org/10.1017/jfm.2025.10934 Published online by Cambridge University Press

Direction	$x \times y$	N_x	N_y	Δ_t
Outward	$[-200, 200] \times [-200, 200]$	2800	2800	10^{-2}
Inward	$[-200, 200] \times [-200, 200]$	2800	2800	10^{-2}

Table 3. Computation parameters for the 2-D Boussinesq–Peregrine system simulations of ring waves.

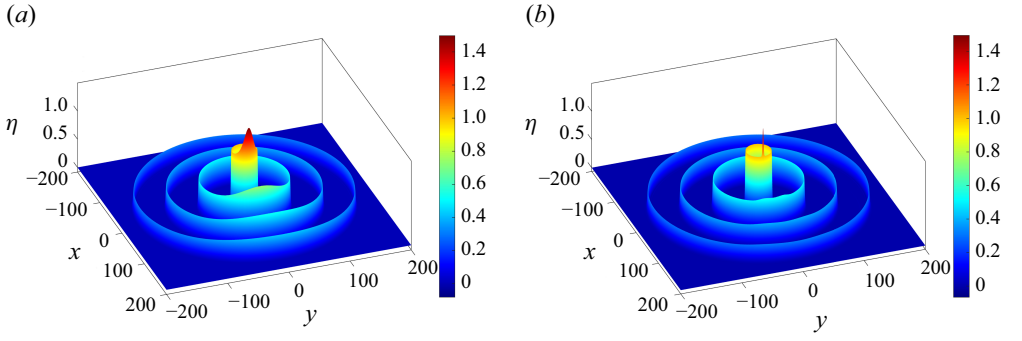


Figure 6. Two-dimensional plots of an outward-propagating perturbed ring wave plotted at the times $t = 0$, 50, 100, 150 for $\beta = 2$ (a) and $\beta = 20$ (b), where $\alpha = 0.5$, $\tilde{v} = 0.5$, $r_0 = 20$, $\epsilon = 0.01$ and $t \in [0, 150]$.

Next, we consider the initial condition with a localised perturbation for the 2-D Boussinesq–Peregrine system (2.1) and (2.2) in the form

$$\eta(t_0, x, y) = 2\tilde{v}\big(1 + \alpha H(x)\,\mathrm{sech}^2\,\beta y\big)\,\mathrm{sech}^2\left(\frac{1}{2}\sqrt{6\tilde{v}}\left[\sqrt{x^2+y^2} - (1+\epsilon\tilde{v})t_0 - r_0\right]\right), \tag{4.2}$$

$$u(t_0, x, y) = \frac{x}{\sqrt{x^2+y^2}}\,\eta(t_0, x, y), \qquad v(t_0, x, y) = \frac{y}{\sqrt{x^2+y^2}}\,\eta(t_0.x, y), \tag{4.3}$$

where α and β control the amplitude and width of the perturbation, respectively, and $H = H(x)$ is the Heaviside function to only give the perturbation on one side of the ring. At the origin of the xy plane, we set $\eta(t_0, 0, 0) = u(t_0, 0, 0) = v(t_0, 0, 0) = 0$ to avoid division by zero, and, for all ring-wave simulations, we use the computation parameters in table 3.

For the outward-propagating ring wave, we solve the 2-D Boussinesq–Peregrine system for $t \in [0, 150]$, $\epsilon = 0.01$, $r_0 = 20$, $\tilde{v} = 0.5$ and $\alpha = 0.5$ for the two values of β shown, and the computation parameters in table 3 give figure 6.

We consider two perturbations. The wider perturbation, with $\beta = 2$, has a width comparable to the radius of the initial ring. It expands and decreases in amplitude as the wave radially diverges. The narrower perturbation, with $\beta = 20$, has a width comparable to the wavelength of the concentric wave. It instead rapidly splits and travels sideways along the wavefront, eventually becoming unnoticeable. Both outward-propagating perturbed ring waves are stable.

To generate inward-propagating ring waves in the 2-D Boussinesq–Peregrine system, we multiply the velocities (4.3) by -1, to reverse the direction of propagation. We then solve this system for $t \in [0, 250]$, $\epsilon = 0.01$, $r_0 = 180$, $\tilde{v} = 0.5$ and $\alpha = 0.5$ for the two values of β shown, and the computation parameters listed in table 3. The results are shown in figures 7 and 8.

https://doi.org/10.1017/jfm.2025.10934 Published online by Cambridge University Press

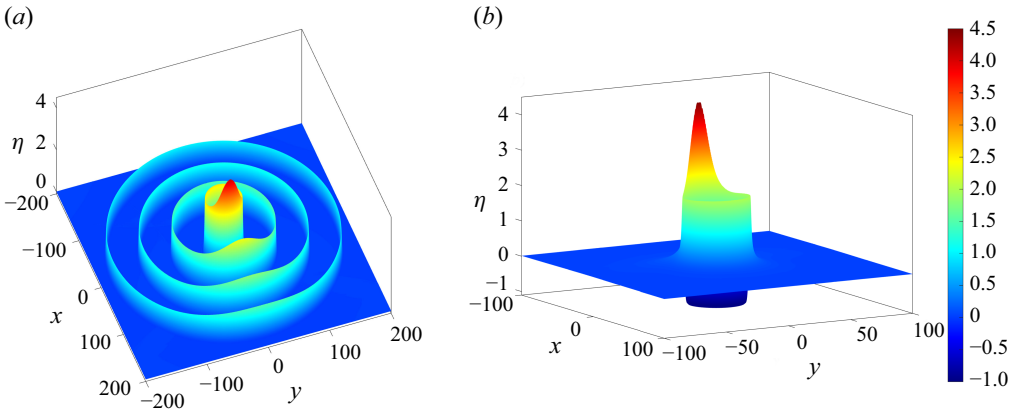


Figure 7. Two-dimensional plots of an inward-propagating perturbed ring wave plotted at the times $t = 0$, 50, 100, 150 (a) and $t = 200$ (b), where $\alpha = 0.5$, $\beta = 2$, $\tilde{v} = 0.5$, $r_0 = 180$, $\epsilon = 0.01$ and $t \in [0, 250]$.

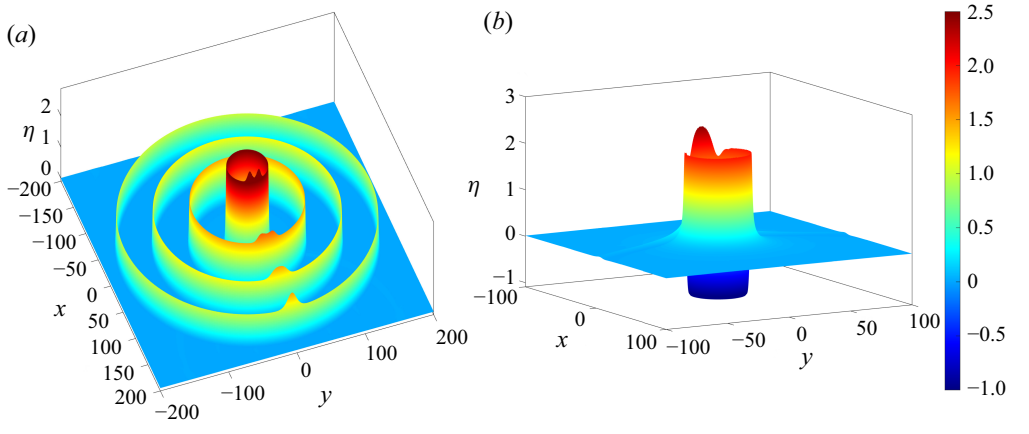


Figure 8. Two-dimensional plots of an inward-propagating perturbed ring wave plotted at the times $t = 0$, 50, 100, 150 (a) and $t = 200$ (b), where $\alpha = 0.5$, $\beta = 20$, $\tilde{v} = 0.5$, $r_0 = 180$, $\epsilon = 0.01$ and $t \in [0, 250]$.

The wider perturbation, with $\beta = 2$, comparable to the radius of the ring, focuses to a point without splitting. The narrower perturbation, with $\beta = 20$, comparable to the wavelength, splits, taking longer to do so than its outward-propagating counterpart. In both figures 7 and 8 the wave propagates through the origin and reforms the general shape as before, with the perturbation seemingly remaining on the same path, now as an outward-propagating perturbed ring wave. The case of the narrower ($\beta = 20$) perturbation has more radiation on the trailing edge of the wave compared with the wider ($\beta = 2$) perturbation case. When the perturbation is narrower, and once it has passed through the origin, the perturbation starts to deform the shape of the ring, as seen in figure 9. However, when the wave is at the origin, with the maximum amplitude $||\eta||_\infty = 44.12$ occurring at $t = 177.5$, the wave is almost concentric. Once the wave has passed through the origin, it retains the form of the perturbation, now as an outward-propagating perturbed ring wave. The wavefront is constantly radiating small waves, and the moustache-shaped radiation from the perturbation is clearly visible in both figures 8 and 9. Once the wave has propagated sufficiently far outward, it retains its concentric shape.

https://doi.org/10.1017/jfm.2025.10934 Published online by Cambridge University Press

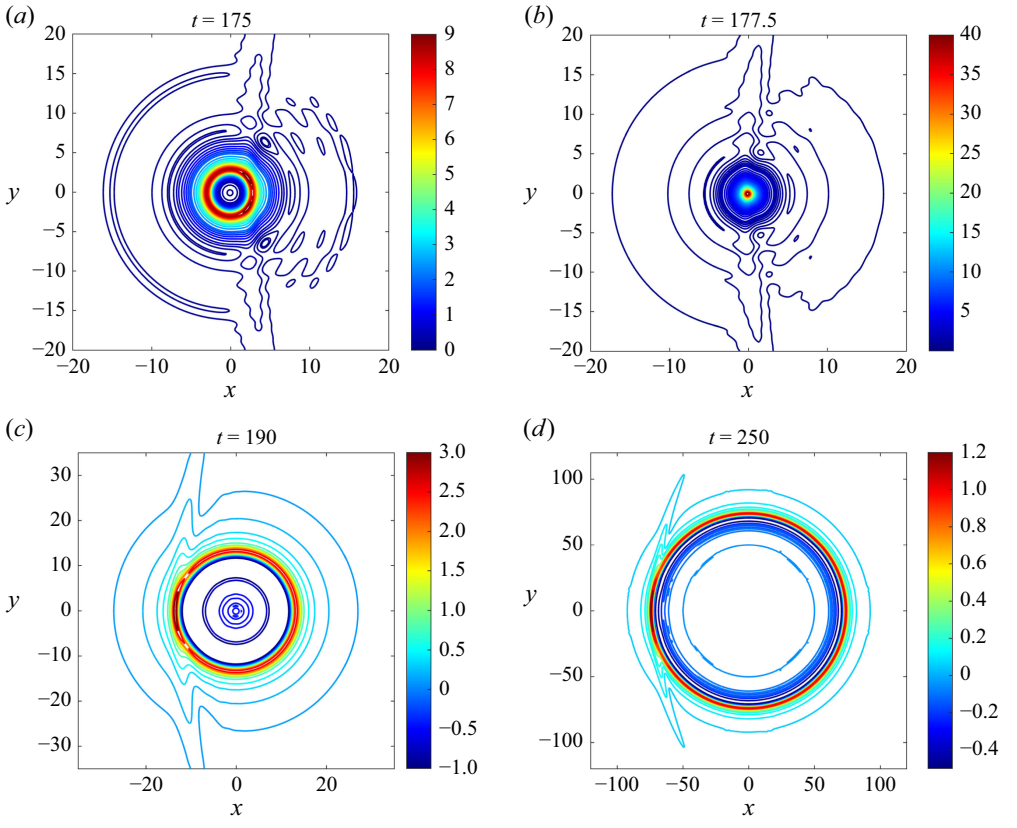


Figure 9. Contour plots of the inward-propagating perturbed ring wave from figure 8 before (a), during (b) and after (c,d) the propagation through the origin, where $\alpha = 0.5$, $\beta = 20$, $\tilde{v} = 0.5$, $r_0 = 180$, $\epsilon = 0.01$.

We now apply a periodic perturbation to the inward-propagating ring wave. Theoretical considerations by Ostrovskii & Shrira (1976), Shrira & Pesenson (1984), Pesenson (1991) suggest that there exists a critical wavelength of the perturbation, such that above this wavelength, the perturbed ring wave is unstable, whereas below this critical value, it is stable. However, an analytical formula for this critical wavelength is not available at present, and deriving it is a separate problem beyond the scope of the present study. Here, in the first numerical study of the problem, we aim to provide an illustrative example of this qualitative difference. Taking the initial condition

$$\eta(t_0, x, y) = 2\tilde{v}\left(1.25 + \alpha \cos\left(\beta \arctan\frac{y}{x}\right)\right) \operatorname{sech}^2\left(\frac{1}{2}\sqrt{6\tilde{v}}\left[\sqrt{x^2+y^2} - x_0\right]\right), \quad (4.4)$$

$$u(t_0, x, y) = -\frac{x}{\sqrt{x^2+y^2}}\,\eta(t_0, x, y), \qquad v(t_0, x, y) = -\frac{y}{\sqrt{x^2+y^2}}\,\eta(t_0, x, y), \quad (4.5)$$

we solve the 2-D Boussinesq–Peregrine system (2.1) and (2.2) for $t \in [0, 150]$, $\epsilon = 0.01$, $\tilde{v} = 0.5$ and $\alpha = 0.5$ for $\beta = 20$ and $\beta = 4$, and the computation parameters listed in table 3. The results are shown in figure 10.

It is clear that the higher-frequency periodic perturbation does not grow faster than the rate of the radial convergence, whereas the low-frequency counterpart does. Both cases produce periodic radiation patterns around the ring. However, the higher-frequency perturbation radiates considerably more, as seen in figure 10, but remains largely

https://doi.org/10.1017/jfm.2025.10934 Published online by Cambridge University Press

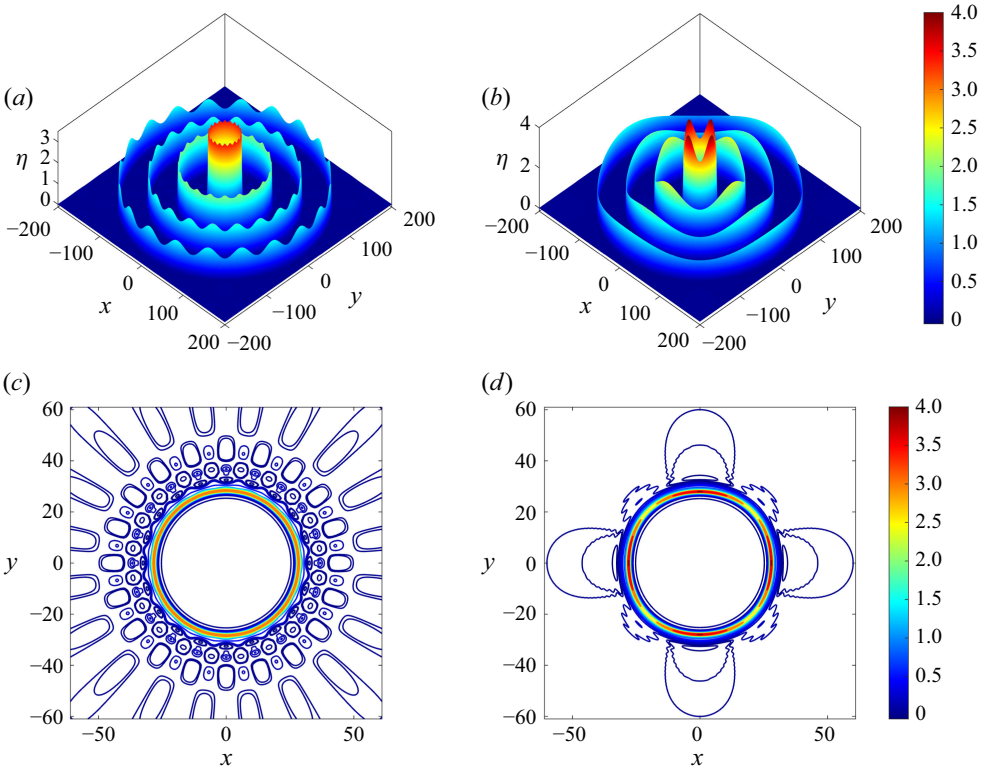


Figure 10. Two-dimensional (*a*,*b*) and contour (*c*,*d*) plots of an inward-propagating periodically perturbed ring wave for $\beta = 20$ (*a*,*c*) and $\beta = 4$ (*b*,*d*), where $\alpha = 0.5$, $\tilde{v} = 0.5$, $r_0 = 180$, $\epsilon = 0.01$ and $t \in [0, 150]$. The 2-D plots (*a*,*b*) are plotted at the times $t = 0$, 50, 100, 150 and the corresponding contour plots (*c*) and (*d*) are plotted at $t = 150$.

concentric, in contrast to the low-frequency perturbation, which notably deforms the ring. Hence, our simulations show significant qualitative differences in the behaviour of these two perturbations.

5. Pure and perturbed hybrid waves

In this section we construct and model hybrid waves, generated by initial conditions formed by an arc of a ring wave and two tangent plane waves (Ostrovskii & Shrira 1976; Hooper *et al.* 2021). The two regions are constructed using the same description for plane and ring waves as above, and the wavefront has a continuous derivative. Surface signatures of similarly looking internal waves generated in the Strait of Gibraltar can be seen in the SAR images shown in figure 1, as well as figures 13 and 14 of Apel (2003). As discussed in the introduction, all considerations of our present work can be extended to internal waves and to parallel shear flows.

We use the exact solution of the KdVθ equation given by

$$\eta(T, \xi, \theta) = 2\tilde{v}\,\mathrm{sech}^2\left(\frac{1}{2}\sqrt{6\tilde{v}}\left[\xi - \tilde{v}T - \xi_0\right]\right), \tag{5.1}$$

where $\xi = rk(\theta) - st$, $T = \epsilon t$, to define the plane-wave sections of a hybrid wave. We match the two plane waves to an arc of a ring wave centred at the origin at the polar angles $\theta = \pm\varphi$.

https://doi.org/10.1017/jfm.2025.10934 Published online by Cambridge University Press

Regime	Direction	$x \times y$	N_x	N_y	Δ_t
2D Boussinesq	Outward	$[50, 350] \times [-250, 250]$	2400	4000	10^{-2}
2D Boussinesq	Inward	$[-220, 130] \times [-250, 250]$	2800	4000	10^{-2}
Regime	Direction	$\xi \times Y$	N_ξ	N_Y	Δ_T
KPII	Outward	$[0, 300] \times [-30, 30]$	2800	4000	10^{-3}
KPII	Inward	$[-200, 250] \times [-30, 30]$	2250	1500	10^{-3}

Table 4. Computation parameters for the 2-D Boussinesq–Peregrine system and KPII equation simulation of hybrid waves.

The plane-wave sections are defined for $|y| \geqslant x \tan\varphi$ and we use the general solution of (1.12), $k(\theta) = a\cos\theta + b(a)\sin\theta$, and hence $\xi = ax + b(a)y - t$, with $a = \cos\varphi$ and $b(a) = \sin\varphi$. In the xy plane, using the Cartesian velocities (2.24), the initial condition becomes

$$\eta(t_0, x, y) = 2\tilde{v}\,\mathrm{sech}^2\left(\frac{1}{2}\sqrt{6\tilde{v}}\left[ax \pm b(a)y - (1+\epsilon\tilde{v})t_0 - \xi_0\right]\right), \tag{5.2}$$

$$u(t_0, x, y) = \cos\varphi\,\eta(t_0, x, y), \quad v(t_0, x, y) = \pm\sin\varphi\,\eta(t_0, x, y_0), \tag{5.3}$$

where the upper and lower signs in η and the velocity v are for the upper and lower plane-wave sections, respectively.

For $|y| < x\tan\varphi$, we take $k(\theta)$ to be the singular solution of (1.12), i.e. the geometrical envelope of the general solution, giving $k(\theta) = 1$, and hence $\xi = r - t$. Therefore, in the xy plane, the ring-wave part of the initial condition is given by

$$\eta(t_0, x, y) = 2\tilde{v}\,\mathrm{sech}^2\left(\frac{1}{2}\sqrt{6\tilde{v}}\left[\sqrt{x^2+y^2} - (1+\epsilon\tilde{v})t_0 - r_0\right]\right), \tag{5.4}$$

$$u(t_0, x, y) = \frac{x}{\sqrt{x^2+y^2}}\,\eta(t_0, x, y), \quad v(t_0, x, y) = \frac{y}{\sqrt{x^2+y^2}}\,\eta(t_0, x, y). \tag{5.5}$$

The initial condition is therefore defined in the entire xy plane, and we match the sections by choosing the constants $\xi_0 = r_0$, so that at the initial moment of time there is a smooth transition between plane and ring parts at $\theta = \pm\varphi$.

We modify the initial conditions to bring them to zero near the boundaries by multiplying them by the double tanh-function $M_x(x)M_y(y)$, where

$$M_x(x) = \frac{1}{2}\left[\tanh\kappa(x - x_{min} - x_{span}) - \tanh\kappa(x - x_{max} + x_{span})\right], \tag{5.6}$$

$$M_y(y) = \frac{1}{2}\left[\tanh\kappa(y - y_{min} - y_{span}) - \tanh\kappa(y - y_{max} + y_{span})\right], \tag{5.7}$$

to maintain the periodic boundary conditions during our pseudospectral numerical runs. Typically, we take the parameter values $\kappa = 0.25$, $x_{span} = (x_{max} - x_{min})/20$ and $y_{span} = (y_{max} - y_{min})/20$. Such modification to the amplitude generates cylindrical radiation at the ends of the legs, similar to that described by Yuan & Wang (2022), and we ensure that the computational domain is sufficiently large, so that these artefacts do not affect the central region. We solve the 2-D Boussinesq–Peregrine system (2.1) and (2.2) for $t \in [0, 150]$, $\epsilon = 0.01$, $\tilde{v} = 0.5$, $r_0 = 150$ and computation parameters listed in table 4. The results are shown in figure 11.

The initial condition evolves into a wavefront with three distinct sections and a small amount of radiation, not visible here in figure 11. The plane-wave legs propagate with

https://doi.org/10.1017/jfm.2025.10934 Published online by Cambridge University Press

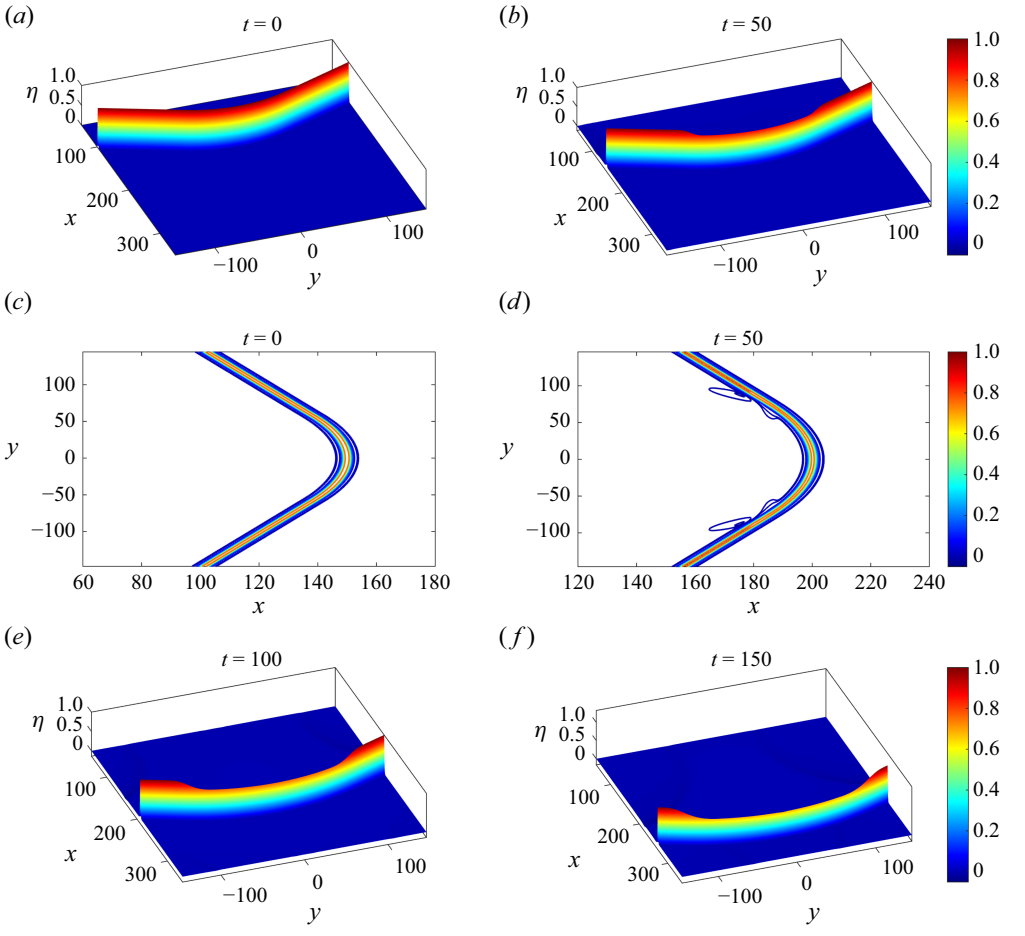


Figure 11. Two-dimensional (*a*,*b*,*e*,*f*) and contour (*c*,*d*) plots of an outward-propagating hybrid wave in the 2-D Boussinesq–Peregrine system, where $\tilde{v} = 0.5$, $r_0 = 150$, $\varphi = \pm\pi/8$, $\epsilon = 0.01$ and $t \in [0, 150]$.

constant amplitude, retaining their shape, and are well described by the exact soliton solution (5.2) and (5.3), obtained using the KdVθ equation (3.7). The amplitude of the ring-wave section gradually decreases due to the radial divergence and, provided the wave is sufficiently far from the origin, it is well described by the cKdV equation (2.36) (Sidorovas *et al.* 2024). The third section is the transition region between the legs and the central ring wave. It is not described by either the KdVθ or cKdV equations, but is described by the KPII equation (2.47) and, potentially, the modulation theory of Biondini, Hoefer & Moro (2020), Ryskamp *et al.* (2021) could also be extended to describe this region.

This outward-propagating hybrid wave can be described using the KPII equation (2.47). To do so, one must rewrite the initial conditions and relevant regions using the KPII variables $T = \epsilon t$, $\xi = x - t$ and $Y = \sqrt{\epsilon} y$. The plane-wave section ($|y| \geqslant x \tan\varphi$) is mapped to $|Y| \geqslant \sqrt{\epsilon}(\xi + T_0/\epsilon)\tan\varphi$, where the surface elevation (5.2) is given by

$$\tilde{\eta}(T_0, \xi, Y) = 2\tilde{v}\,\mathrm{sech}^2\left(\frac{1}{2}\sqrt{6\tilde{v}}\left[a\xi + \frac{b(a)}{\sqrt{\epsilon}}Y - \left(\tilde{v} + \frac{1-a}{\epsilon}\right)T_0 - r_0\right]\right). \tag{5.8}$$

https://doi.org/10.1017/jfm.2025.10934 Published online by Cambridge University Press

The ring-wave section ($|y| < x\tan\varphi$) is mapped to $|Y| < \sqrt{\epsilon}(\xi + T_0/\epsilon)\tan\varphi$, where the surface elevation (5.4) is given by

$$\tilde{\eta}(T_0, \xi, Y) = 2\tilde{v}\,\mathrm{sech}^2\left(\frac{1}{2}\sqrt{6\tilde{v}}\left[\sqrt{\left(\xi + \frac{T_0}{\epsilon}\right)^2 + \frac{Y^2}{\epsilon}} - \left(\tilde{v} + \frac{1}{\epsilon}\right)T_0 - r_0\right]\right). \tag{5.9}$$

Initial conditions for the KPII equation must have zero mass (Klein, Sparber & Markowich 2007; Biondini, Bivolcic & Hoefer 2025). To abide by this constraint, we modify the initial condition $\tilde{\eta}$ by adding, for each Y_i in the Y domain, a pedestal of the form

$$p_i = \frac{p_0}{2}\left(\tanh\kappa(\xi - \xi_{min} - \xi_{span}) - \tanh\kappa(\xi - \xi_{max} - \xi_{span})\right), \tag{5.10}$$

where p_0 and κ are some suitable constants. One can then define the massless initial condition to be

$$\eta(T_0, \xi, Y_i) = \tilde{\eta}(T_0, \xi, Y_i) - p_i(\xi), \tag{5.11}$$

where

$$\int_{\xi_{min}}^{\xi_{max}} \tilde{\eta}(T_0, \xi, Y_i)\,\mathrm{d}\xi = \int_{\xi_{min}}^{\xi_{max}} p_i(\xi)\,\mathrm{d}\xi. \tag{5.12}$$

We usually take $\kappa = 0.5$, $\xi_{span} = (\xi_{max} - \xi_{min})/20$. In practice, due to the size of the domain, this leads to a pedestal of amplitude less than ϵ, and therefore, the effect on the numerical solution is negligible. Further discussion of the numerical solution to the KPII equation is given in Appendix B.

As the outward-propagating hybrid wave moves away from the origin, the effects of cylindrical divergence are weak and the wavefront propagates in a quasi-stationary manner. The description of the central part of the wavefront can therefore be given analytically using the asymptotic solution constructed by Johnson (1999). It is given for the initial-value problem

$$2\eta_T + 3\eta\eta_\xi + \frac{1}{3}\eta_{\xi\xi\xi} + \frac{\eta}{T} = 0, \quad \eta(T_0, \xi) = A\,\mathrm{sech}^2\left(\frac{\sqrt{3A}}{2}\xi\right), \tag{5.13}$$

which is posed sufficiently far away from the origin, and then the radial-divergence term can be viewed as a perturbation of the KdV equation. The three components of the wave are the primary wave, the shelf and the transition region leading back to the undisturbed medium. The variables

$$\sigma = T_0^{-1}, \quad X = \sigma T, \quad \mathcal{T} = \frac{1}{2}\sqrt{3AX^{-\frac{2}{3}}}, \quad f(X) = \frac{3}{2}A\left(X^{\frac{1}{3}} - 1\right), \tag{5.14}$$

$$\Theta = \xi - \sigma^{-1}f(X), \quad \bar{s} = \mathrm{sech}(\mathcal{T}\Theta), \quad \bar{t} = \tanh(\mathcal{T}\Theta) \tag{5.15}$$

are required to construct the three components. The primary wave is given by

$$\eta_{primary} = AX^{-\frac{2}{3}}\bar{s}^2 + \frac{2\sigma}{3}\frac{X^{-\frac{2}{3}}}{\sqrt{3A}}\left[-1 + \bar{t} + (3 + 2\mathcal{T}\Theta)\bar{s}^2 - \left(\frac{35}{12} + 3\mathcal{T}\Theta + \mathcal{T}^2\Theta^2\right)\bar{t}\bar{s}^2\right], \tag{5.16}$$

the shelf is described by

$$\eta_{shelf} = AX^{-\frac{2}{3}}\bar{s}^2 - \frac{4\sigma}{3}(3A + 2\sigma\xi)^{-\frac{1}{2}} \tag{5.17}$$

https://doi.org/10.1017/jfm.2025.10934 Published online by Cambridge University Press

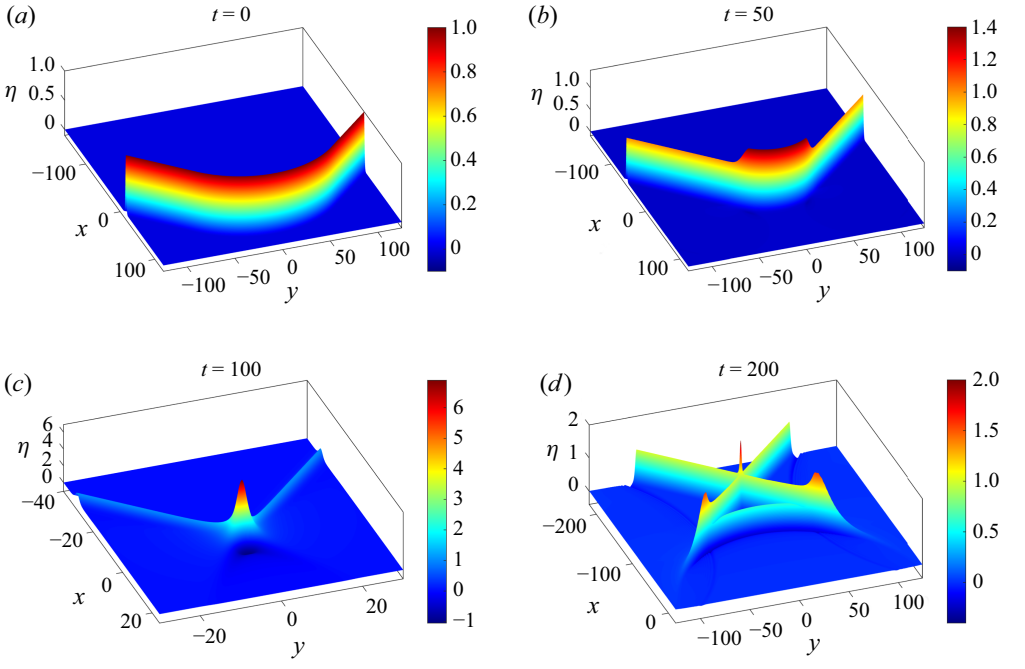


Figure 12. Two-dimensional plots of an inward-propagating hybrid wave in the 2-D Boussinesq–Peregrine equations, where $\tilde{v} = 0.5$, $r_0 = 100$, $\varphi = \pm\pi/4$, $\epsilon = 0.01$ and $t \in [0, 150]$.

and, finally, the transition region is given in the form

$$\eta_{transition} = AX^{-\frac{2}{3}}\bar{s}^2 - \frac{4\sigma}{3}(3A)^{-\frac{1}{2}}\left(1 - \int_{\xi(2\sigma/X)^{1/3}}^{\infty} Ai(\xi')\,\mathrm{d}\xi'\right), \tag{5.18}$$

where Ai is the Airy function. The three components can be used to describe the central part of the hybrid wave in (T, ξ) space for suitably small σ and, hence, suitably large T_0. This asymptotic solution was tested for a pure ring wave by Sidorovas *et al.* (2024), and therefore, is applicable in the central part of the hybrid wave, which is well described by the cKdV equation. Hence, one can describe analytically the three main parts of the outward-propagating hybrid wave: the two legs and the central region.

We now model the inward-propagating hybrid wave. The wave is generated by the same set of initial conditions, (5.2)–(5.5), in the same regions. However, the velocities are multiplied by -1, to reverse the direction of propagation, and similarly brought to zero near the boundaries. We solve the 2-D Boussinesq–Peregrine system (2.1) and (2.2) for $t \in [0, 150]$, $\epsilon = 0.01$, $\tilde{v} = 0.5$, $r_0 = 100$ and the computation parameters listed in table 4. The results are shown in figures 12–14.

The intermediate evolution of the wavefront is dominated by the ring-wave section focusing in on itself, increasing the amplitude dramatically, as shown by the L^∞ norm in figure 13. However, this is not a finite-time blow-up of the numerical solution, since, as the resolution of the mesh is increased, the amplitude converges to a consistent value for the same t value. The converging wavefront generates a large rogue wave (lump), which subsequently disintegrates into three pieces and eventually generates a stable 'X-type' formation, similar to that observed within the scope of the KPII equation in figure 1 of Ablowitz & Baldwin (2012) and studied in Chakravarty & Kodama (2009, 2014); Chakravarty, Lewkow & Maruno (2010). There also exists an arc of opposite curvature

https://doi.org/10.1017/jfm.2025.10934 Published online by Cambridge University Press

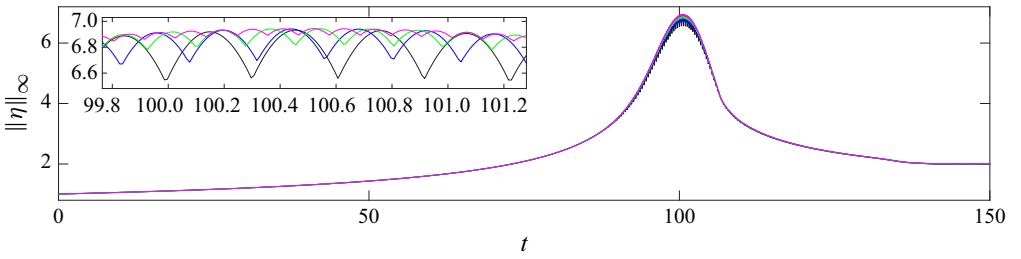


Figure 13. The L^∞ norm of η for the inward-propagating hybrid wave, where $\tilde{v} = 0.5$, $r_0 = 100$, $\varphi = \pi/4$, $\epsilon = 0.01$ and $t \in [0, 150]$. The results are shown for the varying computational grid sizes $\Delta_x = \Delta_y = 0.35$ (black), $\Delta_x = \Delta_y = 0.275$ (blue), $\Delta_x = \Delta_y = 0.2$ (green) and $\Delta_x = \Delta_y = 0.125$ (magenta).

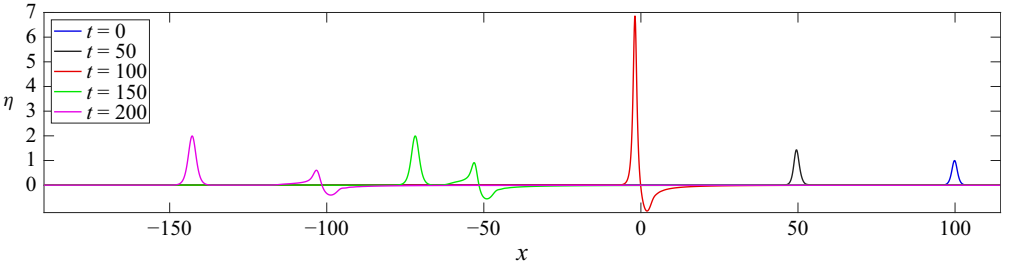


Figure 14. Cross-section plot along $x = 0$ of the domain from figure 12 plotted five times from $t = 0$ to $t = 200$.

to the initial condition connecting two lump-like structures on the legs behind the X. Previous studies have focused on 'V-type' initial data for the KPII equation rather than our hybrid wave formation. These studies have shown similar X-type structures obtained numerically without a noticeable phase shift, see, for example, Chakravarty & Kodama (2009), Ryskamp *et al.* (2021), Ryskamp, Hoefer & Biondini (2022). A weaker arc of opposite curvature to the initial condition connecting the two legs was observed by Yuan *et al.* (2018*a*), Ryskamp *et al.* (2021) in the KPII equation and from the cross-section in figure 14 has a shape similar to the plane-wave derivative. The effect of curvature on the amplitude of the generated waves was noted in Porubov *et al.* (2005). To the best of our knowledge, the overall behaviour of the inward-propagating hybrid wave, including the generation of the large rogue wave and its disintegration into the three pieces, with the subsequent formation of the X wave, has not been reported in any previous studies. Although the KPII equation does not support the exact lump solutions, unlike the KPI equation, our study shows that lumps, understood as localised 2-D waves, can exist as transient (emerging and then disappearing) features in the evolution of curved solitons, contributing to the mechanisms of generation of rogue waves (see, for example, Shrira & Pesenson 1984; Kharif, Pelinovsky & Slunyaev 2008; Onorato *et al.* 2013; He & Chabchoub 2025; Nirunwiroj, Tseluiko & Khusnutdinova 2025 and references therein).

It turns out that the X-type wave formed at the end can be described by the solution of the KPII equation discussed, in a different context, by Ablowitz & Baldwin (2012):

$$\eta = \frac{4}{3}\frac{\partial^2}{\partial \xi^2} \log(F_2). \tag{5.19}$$

https://doi.org/10.1017/jfm.2025.10934 Published online by Cambridge University Press

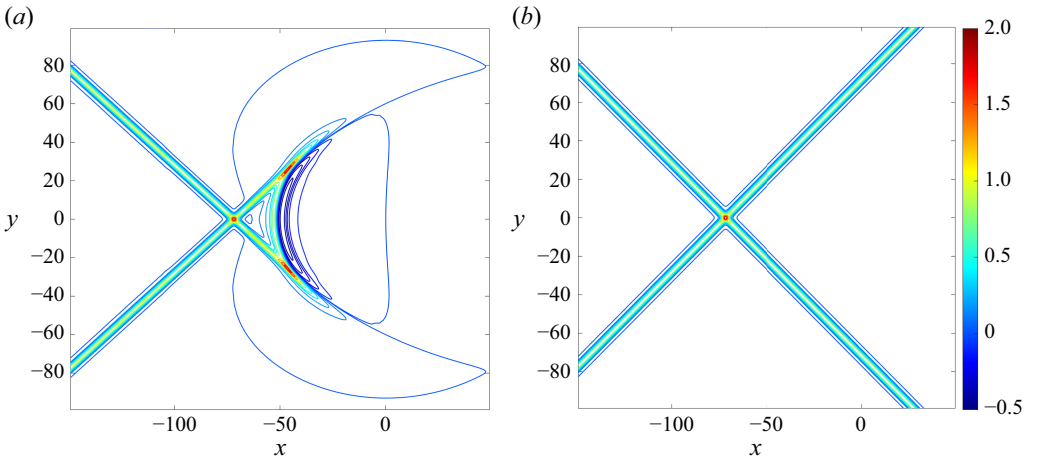


Figure 15. Contour plots of (*a*) the inward-propagating hybrid wave at $t = 150$ from figure 12 and (*b*) the parameter-matched '*X*-type' two-soliton solution of the KPII equation.

Here

$$F_2 = 1 + e^{\eta_1} + e^{\eta_2} + e^{\eta_1+\eta_2+A_{12}}, \tag{5.20}$$

$$\eta_i = 6k_i\left(\xi + 6P_iY - 6\left(k_i^2 + 3P_i^2\right)T\right) + c_i, \quad i = 1, 2, \tag{5.21}$$

$$e^{A_{12}} = \frac{(k_1 - k_2)^2 - (P_1 - P_2)^2}{(k_1 + k_2)^2 - (P_1 - P_2)^2}, \tag{5.22}$$

such that k_i and P_i are constants determining the propagation angle and c_i is an arbitrary constant shifting the wavefront. For our numerical run, the crossing angle is $\pi/4$, and good agreement is obtained for the parameter values $6k_1 = 6k_2 = 1.1314$, $6P_1 = -6P_2 = \epsilon^{-1/2}$ and $c_1 = c_2 = 71.75k_1$. The value of $e^{A_{12}}$ is indicative of the behaviour of the wavefront where the two solitons cross. For the case seen here, $e^{A_{12}} = 1.013$, implying an *X*-type interaction with a very short stem between the legs, as seen from the evolved state of the inward-propagating hybrid wavefront. Indeed, there is no observable phase shift and the comparison between the KPII two-soliton solution and the inward-propagating hybrid wave is given in figure 15. The amplitude of the two-soliton cross depends on the propagation angle, and a discussion on how to obtain the maximum of the cross is discussed by Chakravarty *et al.* (2010).

To model the entire process of the inward-propagating hybrid wave seen in figure 12 with the KPII equation, we must first reverse the direction of propagation. Therefore, for T reducing, we map $t \to -t$ and, hence, $\partial/\partial T = -\partial/\partial T$ and $\xi \to \zeta = x + t$, which yields the inward-propagating KPII equation

$$\left(2\eta_T - 3\eta\eta_\zeta - \frac{1}{3}\eta_{\zeta\zeta\zeta}\right)_\zeta - \eta_{YY} = 0. \tag{5.23}$$

The initial condition for the plane-wave section ($|y| \geqslant x\tan\varphi$) is defined when $|Y| \geqslant \sqrt{\epsilon}(\zeta - T_0/\epsilon)\tan\varphi$ and is given by

$$\tilde{\eta}(T_0, \zeta, Y) = 2\tilde{v}\,\mathrm{sech}^2\left(\frac{1}{2}\sqrt{6\tilde{v}}\left[a\zeta + \frac{b(a)}{\sqrt{\epsilon}}Y - \left(\tilde{v} + \frac{1+a}{\epsilon}\right)T_0 - \xi_0\right]\right), \tag{5.24}$$

https://doi.org/10.1017/jfm.2025.10934 Published online by Cambridge University Press

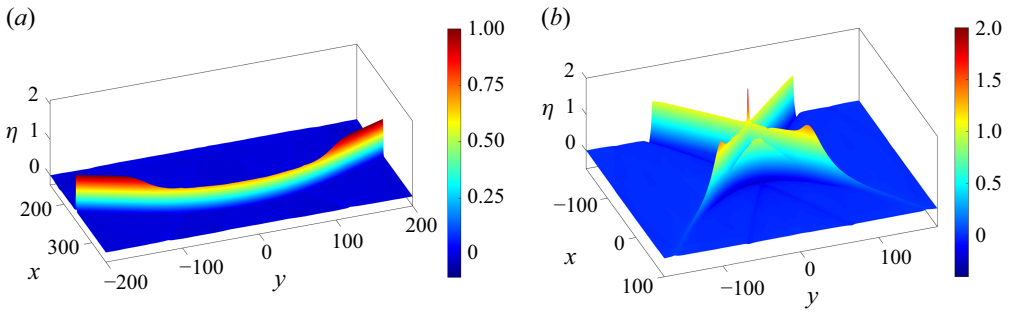


Figure 16. Two-dimensional plots of the numerical solution to the KPII equation for both the outward- (*a*) and inward- (*b*) propagating hybrid waves for $\varphi = \pi/8$, $r_0 = 150$ (*a*) and $\varphi = \pi/4$, $r_0 = 100$ (*b*) at $|T| = 1.5$, where $\tilde{v} = 0.5$, $\epsilon = 0.01$ and $|T| \in [0, 1.5]$.

and the ring-wave section ($|y| < x \tan\varphi$), defined when $|Y| < \sqrt{\epsilon}(\zeta - T_0/\epsilon)\tan\varphi$, is given by

$$\tilde{\eta}(T_0, \zeta, Y) = 2\tilde{v}\,\mathrm{sech}^2\left(\frac{1}{2}\sqrt{6\tilde{v}}\left[\sqrt{\left(\zeta - \frac{T_0}{\epsilon}\right)^2 + \frac{Y^2}{\epsilon}} - \left(\tilde{v} + \frac{1}{\epsilon}\right)T_0 - \xi_0\right]\right), \quad (5.25)$$

where, before solving, the mass of the solution should be removed to satisfy the zero-mass constraint of the KPII equation as before, such that $\eta = \tilde{\eta} - p(\xi)$ for the pedestal $p(\xi)$. Solving (2.47) and (5.23) with the initial data of (5.8), (5.9) and (5.24), (5.25), respectively, for the parameter values given to match figures 11 and 12, we obtain the results that are shown in figure 16.

We see that the computations give all of the same structures as those observed in the 2-D Boussinesq–Peregrine system, up to the accuracy of the reduced model. Notably, the transient lump-like structures in the middle and at the ends of the legs are present, as in figure 12, despite the fact that the KPII equation for weak surface tension used here does not possess lump soliton solutions. These transient lumps constantly decrease in amplitude, converting their energy to extend the legs behind the X. We also note that some radiation escapes and re-enters the periodic domain of the numerical solver, causing some small defects. The inclusion of a sponge layer can remove these artefacts.

Finally, in this section we model the evolution of an inward-propagating perturbed hybrid wave. We choose to apply a periodic perturbation to the ring-wave section, altering (5.4) and (5.5) but keeping (5.2) and (5.3) unchanged. We again take the velocities to be negative for inward propagation. We perturb the arc of a ring wave in the region $|y| < x\tan\varphi$ to be given by

$$\eta(t_0, x, y) = \left(\frac{3}{2} + \alpha\cos\left(\beta\arctan\frac{y}{x}\right)\right)\eta_0(t_0, x, y), \quad (5.26)$$

$$u(t_0, x, y) = -\frac{x}{\sqrt{x^2+y^2}}\,\eta(t_0, x, y), \quad v(t_0, x, y) = -\frac{y}{\sqrt{x^2+y^2}}\,\eta(t_0, x, y). \quad (5.27)$$

Solving the 2-D Boussinesq–Peregrine system (2.1) and (2.2) for the perturbed initial condition given by (5.2) and (5.3), and (5.26) and (5.27) for $t \in [0, 150]$, $\epsilon = 0.01$, $\tilde{v} = 0.5$, $r_0 = 100$, $\alpha = 0.5$, $\beta = 12$ and the computation parameters listed in table 4, yields the results shown in figure 17.

The evolution of the inward-propagating perturbed hybrid wave is remarkably similar to that of the unperturbed case, despite the large amplitude and wavelength of the

https://doi.org/10.1017/jfm.2025.10934 Published online by Cambridge University Press

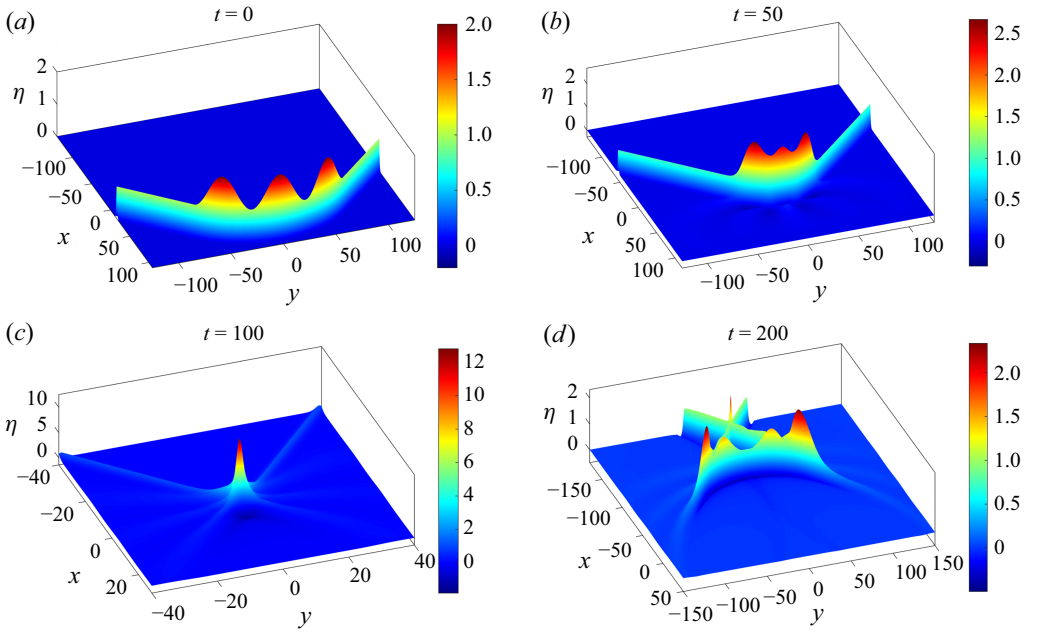


Figure 17. Two-dimensional plots of a perturbed inward-propagating hybrid wave in the 2-D Boussinesq–Peregrine system, where $\alpha = 0.5$, $\beta = 12$, $\tilde{v} = 0.5$, $r_0 = 100$, $\varphi = \pm\pi/4$, $\epsilon = 0.01$ and $t \in [0, 200]$.

perturbation applied. The perturbed hybrid wave also generates a large rogue wave (larger than in the unperturbed case) and still eventually forms a stable X-type cross. The initial radiation behind the ring-wave section is qualitatively similar to that observed in the ring-wave study in § 4. The main difference is that the transient rogue wave disintegrates into more pieces than in the pure hybrid wave evolution.

Finally, we note that the $(2+1)$-dimensional cKdV-type equation (1.7) can be used to initiate hybrid waves in the general case of a stratified fluid with a shear flow (see Hooper *et al.* 2021).

6. Discussion

In this paper we investigated the non-stationary 2-D evolution of perturbed plane, ring and hybrid waves within the scope of the 2-D Boussinesq–Peregrine system (Peregrine 1967) for surface waves in a homogeneous fluid, while simultaneously discussing how to extend the theoretical constructions to the general case of a density stratified fluid with a parallel shear flow. In particular, for the plane-wave evolution, we derived a new amplitude equation, the KdVθ equation (3.3), and showed that this equation can be mapped to the usual KdV equation, but with a θ-dependent initial condition. We showed that this result holds for any stratification, and any parallel shear flow, using the $(2+1)$-dimensional cKdV-type equation derived by Khusnutdinova & Zhang (2016). We then applied the KdVθ equation to describe the evolution of a line soliton subject to a long transverse perturbation. We obtained explicit analytical predictions for the evolution using the IST (Gardner *et al.* 1967), and compared the performance of the reduced model with the results of direct numerical simulations for the 2-D Boussinesq–Peregrine system in order to clarify the range of validity of the model. We showed that the KdVθ equation can be used to describe the intermediate evolution of sufficiently long transverse perturbations of line solitons (up

https://doi.org/10.1017/jfm.2025.10934 Published online by Cambridge University Press

to the moment when the perturbation splits and starts propagating sideways along the wavefront). Up to this point the KdVθ equation accurately describes the behaviour of the solution. Hence, when applicable, the KdVθ equation allows one to consider the initial-value problem, which serves as a useful addition to the KPII equation (e.g. Ablowitz & Segur 1979). Recently, transverse amplitude and phase perturbations to line solitons were modelled numerically in the Serre–Green–Naghdi regime by Gavrilyuk & Klein (2024), and the results are qualitatively similar to plane waves propagating over localised bottom topography (see Bassi *et al.* 2020; Gavrilyuk & Shyue 2024). The new equation could thus find useful applications in these settings.

Next, we modelled the non-axisymmetric evolution of the perturbed ring waves, extending the earlier studies of concentric waves by Chwang & Wu (1977), Sidorovas *et al.* (2024). We considered both localised and periodic perturbations, and modelled the long-time evolution of both outward- and inward-propagating waves. The results related to the cKdV equation (Miles 1977; Johnson 1990, 1999) were used to formulate the basic unperturbed initial conditions, but naturally, the cKdV equation could not be used to model the subsequent non-axisymmetric evolution of the perturbed initial conditions, and we used the direct numerical simulations with the parent system instead. In all our runs, the outward-propagating ring waves were stable, while stability of the inward-propagating waves turned out to be related to the characteristic length of the perturbation. In particular, we illustrated the qualitative theoretical predictions made by Ostrovskii & Shrira (1976), Shrira & Pesenson (1984), Pesenson (1991) and showed the difference between the evolution of ring waves with periodic perturbations of differing wavelength, with the waves of smaller/greater wavelength being stable/unstable, respectively. Deriving an explicit formula for the critical wavelength of the perturbation is an interesting open problem.

Finally, we modelled the evolution of hybrid waves, initially consisting of a part of a ring wave and two tangent plane waves. To the best of our knowledge, this is the first systematic study of such waves. We used the results related to the KdVθ, cKdV and KPII equations in order to initiate our 2-D simulations, and to describe the key features of the evolution. The outward-propagating hybrid waves were found to be stable and, when generated sufficiently far away from the origin (in the far field), propagated as quasi-stationary waves, with the central part slowly decreasing in amplitude due to cylindrical divergence. We note that, for the stable cases, qualitatively similar propagation has been observed from V-type (bent soliton) initial conditions by Chakravarty & Kodama (2009), Yuan *et al.* (2018*a*), Ryskamp *et al.* (2021), Ryskamp *et al.* (2022), Biondini *et al.* (2025). Therefore, it is likely that the key features of the outward-propagating case may be described by Whitham modulation theory (see Biondini *et al.* 2020; Hu, Luo & Wang 2025 and references therein).

The inward-propagating hybrid waves, however, turned out to be unstable, which confirmed the theoretical prediction made, using the ray theory, by Ostrovskii & Shrira (1976). We showed that the developed stage of this instability consisted of three main stages: the generation of a large rogue wave (lump), its subsequent disintegration into several pieces and the formation of the X wave known from the theory of the KPII equation. We found the parameters of the X wave matching our results. Moreover, the key stages of this instability scenario did not change when we subjected the central part to a strong periodic perturbation. Finally, we comment that it would be interesting to extend this work to the case of stratified fluids with a background shear flow (see Khusnutdinova & Zhang 2016; Hooper *et al.* 2021; Tseluiko *et al.* 2023) and to waves of moderate amplitude, which so far have been studied using the extended KdV-type models only in

https://doi.org/10.1017/jfm.2025.10934 Published online by Cambridge University Press

the plane and concentric wave settings (see Sidorovas *et al.* 2024, 2025 and references therein).

Acknowledgements. Karima Khusnutdinova is grateful to Artur Sergeev and Victor Shrira for useful discussions. Benjamin Martin is grateful to Loughborough University for a research studentship.

Funding. This research received no specific grant from any funding agency, commercial or not-for-profit sectors.

Declaration of interests. The authors report no conflict of interest.

Appendix A. Derivation of approximate mechanical balance laws of the 2-D Boussinesq–Peregrine system

We calculate the conserved quantities of the 2-D Boussinesq–Peregrine system in the rectangular domain, $D = \{(x, y)|x_1 \leqslant x \leqslant x_2,\ y_1 \leqslant y \leqslant y_2\}$, where we assume periodic boundary conditions. The derivation of the 2-D Boussinesq–Peregrine system is based on the balance $\delta^2 = O(\epsilon)$ (Peregrine 1967), and so one must keep equivalent orders in the conserved form, up to the accuracy of the derivation.

The conservation of mass in the system is found directly from (2.1). By taking the double integral of (2.1) over D we obtain

$$\frac{\mathrm{d}}{\mathrm{d}t}\iint_D \eta \,\mathrm{d}x\,\mathrm{d}y = -\iint_D \left[((1+\epsilon\eta)u)_x + ((1+\epsilon\eta)v)_y\right] \mathrm{d}x\,\mathrm{d}y, \tag{A1}$$

where u and v are the Cartesian components of the velocity $\boldsymbol{u}$. From Green's theorem, (A1) can be rewritten as the contour integral around the rectangular domain yielding

$$\frac{\mathrm{d}}{\mathrm{d}t}\iint_D \eta \,\mathrm{d}x\,\mathrm{d}y = \oint_C \left[(1+\epsilon\eta)u\,\mathrm{d}x - (1+\epsilon\eta)v\,\mathrm{d}y\right] \tag{A2}$$

$$= \int_{x_1}^{x_2} (1+\epsilon\eta)v|_{y=y_1}\,\mathrm{d}x + \int_{x_2}^{x_1} (1+\epsilon\eta)v|_{y=y_2}\,\mathrm{d}x$$
$$- \int_{y_1}^{y_2} (1+\epsilon\eta)u|_{x=x_2}\,\mathrm{d}y - \int_{y_2}^{y_1} (1+\epsilon\eta)u|_{x=x_1}\,\mathrm{d}y = 0 \tag{A3}$$

due to periodicity of the problem.

The approximate momentum of the system, a vector quantity, is given by the double integral of $(1+\epsilon\eta)\boldsymbol{u}$. To obtain an expression for this quantity, we apply the operator $1 + (\delta^2/3)(\nabla(\nabla\cdot))$ to (2.2) and multiply by $1+\epsilon\eta$, which after rearranging yields

$$(1+\epsilon\eta)u_t = -\epsilon(uu_x + vu_y) - (1+\epsilon\eta)\eta_x + \frac{\delta^2}{3}(\eta_{xxx} + \eta_{xxy}) + O(\epsilon^2, \epsilon\delta^2, \delta^4), \tag{A4}$$

$$(1+\epsilon\eta)v_t = -\epsilon(uv_x + vv_y) - (1+\epsilon\eta)\eta_y + \frac{\delta^2}{3}(\eta_{xyy} + \eta_{yyy}) + O(\epsilon^2, \epsilon\delta^2, \delta^4), \tag{A5}$$

and we also take $\epsilon\boldsymbol{u}$ multiplied by (2.1) to give

$$\epsilon u\eta_t = -\epsilon(uu_x + uv_y) + O(\epsilon^2), \tag{A6}$$

$$\epsilon v\eta_t = -\epsilon(vu_x + vv_y) + O(\epsilon^2). \tag{A7}$$

https://doi.org/10.1017/jfm.2025.10934 Published online by Cambridge University Press

Taking the sum of (A4) and (A6), and (A5) and (A7), respectively, and taking the double integral over the domain we can write the result in the form of a conservation law as

$$\frac{\mathrm{d}}{\mathrm{d}t}\iint_D (1+\epsilon\eta)u\,\mathrm{d}x\mathrm{d}y = \iint_D \left(\left[\frac{\delta^2}{3}(\eta_{xx}+\eta_{xy}) - \eta - \epsilon\left(u^2+\frac{1}{2}\eta^2\right)\right]_x - \epsilon\,[uv]_y\right) + O(\epsilon^2, \epsilon\delta^2, \delta^4), \tag{A8}$$

$$\frac{\mathrm{d}}{\mathrm{d}t}\iint_D (1+\epsilon\eta)v\,\mathrm{d}x\mathrm{d}y = \iint_D \left(\left[\frac{\delta^2}{3}(\eta_{xy}+\eta_{yy}) - \eta - \epsilon\left(v^2+\frac{1}{2}\eta^2\right)\right]_y - \epsilon\,[uv]_x\right) + O(\epsilon^2, \epsilon\delta^2, \delta^4). \tag{A9}$$

We can then rewrite (A8) and (A9) as contour integrals via Green's theorem as

$$\frac{\mathrm{d}}{\mathrm{d}t}\iint_D (1+\epsilon\eta)u\,\mathrm{d}x\mathrm{d}y = \oint_C \left[\left\{\frac{\delta^2}{3}(\eta_{xx}+\eta_{xy}) - \eta - \epsilon\left(u^2+\frac{1}{2}\eta^2\right)\right\}\mathrm{d}y + \epsilon uv\,\mathrm{d}x\right] + O(\epsilon^2, \epsilon\delta^2, \delta^4) \tag{A10}$$

$$= \int_{y_1}^{y_2}\left[\frac{\delta^2}{3}(\eta_{xx}+\eta_{xy}) - \eta - \epsilon\left(u^2+\frac{1}{2}\eta^2\right)\right]_{x=x_2}\mathrm{d}y + \int_{y_2}^{y_1}\left[\frac{\delta^2}{3}(\eta_{xx}+\eta_{xy}) - \eta - \epsilon\left(u^2+\frac{1}{2}\eta^2\right)\right]_{x=x_1}\mathrm{d}y + \int_{x_1}^{x_2} uv|_{y=y_1}\,\mathrm{d}x + \int_{x_2}^{x_1} uv|_{y=y_2}\,\mathrm{d}x + O(\epsilon^2, \epsilon\delta^2, \delta^4) \tag{A11}$$

$$= O(\epsilon^2, \epsilon\delta^2, \delta^4), \tag{A12}$$

$$\frac{\mathrm{d}}{\mathrm{d}t}\iint_D (1+\epsilon\eta)v\,\mathrm{d}x\mathrm{d}y = \oint_C \left[\left\{\eta + \epsilon\left(v^2+\frac{1}{2}\eta^2\right) - \frac{\delta^2}{3}(\eta_{xy}+\eta_{yy})\right\}\mathrm{d}y - \epsilon uv\,\mathrm{d}x\right] + O(\epsilon^2, \epsilon\delta^2, \delta^4) \tag{A13}$$

$$= \int_{x_1}^{x_2}\left[\eta + \epsilon\left(v^2+\frac{1}{2}\eta^2\right) - \frac{\delta^2}{3}(\eta_{xy}+\eta_{yy})\right]_{y=y_1}\mathrm{d}x + \int_{x_2}^{x_1}\left[\eta + \epsilon\left(v^2+\frac{1}{2}\eta^2\right) - \frac{\delta^2}{3}(\eta_{xy}+\eta_{yy})\right]_{y=y_2}\mathrm{d}x - \int_{y_1}^{y_2} uv|_{x=x_2}\,\mathrm{d}y - \int_{y_2}^{y_1} uv|_{x=x_2}\,\mathrm{d}y + O(\epsilon^2, \epsilon\delta^2, \delta^4) \tag{A14}$$

$$= O(\epsilon^2, \epsilon\delta^2, \delta^4). \tag{A15}$$

Hence, momentum is conserved in both the x and y directions to the second order of the expansions used to derive the 2-D Boussinesq–Peregrine system.

The approximate energy of the system is given by the double integral of $(1/2)(u^2+v^2+\eta^2)$. It is therefore necessary to multiply (2.1) by η and (2.2) by $\boldsymbol{u}$ and combine the three subsequent equations. Taking the time derivative of this gives

$$\frac{\mathrm{d}}{\mathrm{d}t}\iint_D \frac{1}{2}(u^2+v^2+\eta^2)\,\mathrm{d}x\mathrm{d}y = -\iint_D \left[(u\eta)_x + (v\eta)_y\right]\mathrm{d}x\mathrm{d}y + O(\epsilon, \delta^2), \tag{A16}$$

https://doi.org/10.1017/jfm.2025.10934 Published online by Cambridge University Press

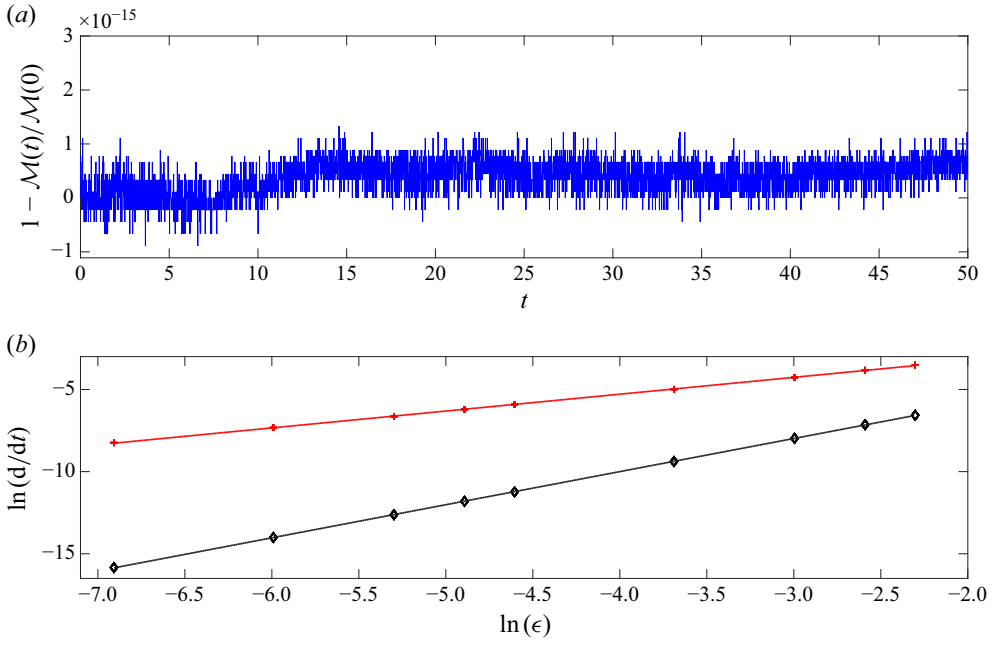


Figure 18. Conservation of mass, momentum and energy for the line-soliton initial condition: (*a*) conservation of mass for $\epsilon = 0.01$ and (*b*) logarithms of the time derivatives of momentum (red) and energy (black) against the logarithm of ϵ at the final computation time $t = 50$. The gradient for energy is 1.025 and for momentum is 2.015.

which we again rewrite as a contour integral around the rectangular computational domain such that

$$\frac{\mathrm{d}}{\mathrm{d}t}\iint_D \frac{1}{2}\left(u^2+v^2+\eta^2\right)\,\mathrm{d}x\mathrm{d}y = \oint_C \left[v\eta\,\mathrm{d}x - u\eta\,\mathrm{d}y\right] + O(\epsilon,\delta^2) \tag{A17}$$

$$= \int_{x_1}^{x_2} v\eta|_{y=y_1}\,\mathrm{d}x + \int_{x_2}^{x_1} v\eta|_{y=y_2}\,\mathrm{d}x - \int_{y_1}^{y_2} u\eta|_{x=x_2}\,\mathrm{d}y - \int_{y_2}^{y_1} u\eta|_{x=x_1}\,\mathrm{d}y = O(\epsilon,\delta^2), \tag{A18}$$

and, hence, the energy is conserved to the first order of the expansions used to derive the 2-D Boussinesq–Peregrine system.

The conservation laws are used to control the quality of our numerical simulations. We illustrate this with an example related to the modelling of the line-soliton initial condition

$$\eta(0,x,y) = 2\tilde{v}\,\mathrm{sech}^2\left(\frac{1}{2}\sqrt{6\tilde{v}}\,[x-x_0]\right), \tag{A19}$$

$$u(0,x,y) = \eta(0,x,y), \tag{A20}$$

$$v(0,x,y) = 0, \tag{A21}$$

with the computation parameters $\tilde{v} = 0.5$, $x_0 = 10$, 640×256 points in the $x \times y$ domain $[0, 80] \times [-20, 20]$ and $N_t = 5000$ for $t \in [0, 50]$. This yields figure 18 for varying values of ϵ from $\epsilon = 0.001$ to $\epsilon = 0.1$.

As shown in figure 18(*a*), the 2-D Boussinesq–Peregrine system conserves the mass of the initial condition to machine double precision, and figure 18(*b*) depicts the logarithms

https://doi.org/10.1017/jfm.2025.10934 Published online by Cambridge University Press

of the time rates of change of momentum and energy at $t = 50$ against $\ln(\epsilon)$. The red and black lines are straight lines obtained by the MATLAB *polyfit* function and have gradients close to 2 and 1, respectively, confirming the $O(\epsilon^2)$ and $O(\epsilon)$ scaling of the rates of change of momentum and energy (see a relevant discussion in Dutykh *et al.* 2013). For all numerical simulations in this paper, the mass, momentum and energy are computed for computation parameters such that the quantities listed above are conserved to the precision of the model.

Appendix B. Numerical method

In this section we discuss the numerical solutions of the KdVθ, KPII and 2-D Boussinesq–Peregrine equations. We use an efficient pseudospectral method where the spatial derivatives are approximated using direct and inverse fast Fourier transforms, and the temporal derivatives are calculated via a fourth-order Runge–Kutta (RK4) scheme for its preferable accuracy.

For a given discretised field η, the derivatives are approximated as

$$\frac{\partial^n \eta}{\partial x^n} = \mathcal{F}^{-1}\left[(ik_x)^n \mathcal{F}[\eta]\right] \quad \text{and} \quad \frac{\partial^n \eta}{\partial y^n} = \mathcal{F}^{-1}\left[(ik_y)^n \mathcal{F}[\eta]\right], \tag{B1}$$

where k_x and k_y are the wavenumbers, $\mathcal{F}$ is the 2-D discrete Fourier transform and $\mathcal{F}^{-1}$ is the 2-D inverse discrete Fourier transform. The wavenumbers for computation are matrices of size $N_y \times N_x$ where the rows of k_x are given by

$$0, 1, \ldots, \frac{N_x}{2}, -\frac{N_x}{2}+1, -\frac{N_x}{2}+2, \ldots, -1, \tag{B2}$$

and the columns of k_y by

$$0, 1, \ldots, \frac{N_y}{2}, -\frac{N_y}{2}+1, -\frac{N_y}{2}+2, \ldots, -1 \tag{B3}$$

(Trefethen 2000). The Fourier transform of a quantity is denoted below as $\mathcal{F}[\eta] = \hat{\eta}$. We solve in an arbitrary rectangular domain, meaning we scale the equation from the domain $[-\pi, \pi] \times [-\pi, \pi]$ to $[x_{min}, x_{max}] \times [y_{min}, y_{max}]$. Performing this scaling has the effect of scaling k_x and k_y wavenumbers by $2\pi/(x_{max} - x_{min})$ and $2\pi/(y_{max} - y_{min})$, respectively. The domains are given by

$$x_i = x_{min} + n\Delta_x, \quad i = 0, 1, \ldots, N_x - 1, \tag{B4}$$

$$y_j = y_{min} + m\Delta_y, \quad j = 0, 1, \ldots, N_y - 1, \tag{B5}$$

such that η, u and v are also discretised into $N_y \times N_x$ grids.

The temporal discretisation used is $\Delta_t = (t_{max} - t_{min})/N_t$ such that $t_n = t_{min} + n\Delta_t$ for $n = 0, 1, \ldots, N_t$, and is computed via the RK4 scheme such that, for a problem in the form

$$\eta_t = f(t, \eta), \tag{B6}$$

the next time step, η^{n+1}, is given as

$$\eta^{n+1} = \eta^n + \frac{\Delta_t}{6}(k_1 + 2k_2 + 2k_3 + k_4), \tag{B7}$$

https://doi.org/10.1017/jfm.2025.10934 Published online by Cambridge University Press

where

$$k_1 = f\left(t_n, \eta^n\right), \quad k_2 = f\left(t_n + \frac{\Delta_t}{2}, \eta^n + \frac{k_1 \Delta_t}{2}\right), \tag{B8}$$

$$k_3 = f\left(t_n + \frac{\Delta_t}{2}, \eta^n + \frac{k_2 \Delta_t}{2}\right), \quad k_4 = f\left(t_n + \Delta_t, \eta^n + k_3 \Delta_t\right). \tag{B9}$$

The 2-D Boussinesq–Peregrine equations are solved using the method presented by Eskilsson & Sherwin (2006), Steinmoeller, Stastna & Lamb (2012) to deal with the two separate time derivatives in (2.2). This is done by introducing a new variable q such that $q = \nabla \cdot \boldsymbol{u}_t$. Upon taking the divergence of (2.2), a third coupled equation is generated, and this gives the following new system of equations with an additional auxiliary equation:

$$\eta_t = -\nabla \cdot \{(1 + \epsilon\eta)\boldsymbol{u}\}, \tag{B10}$$

$$\boldsymbol{u}_t = -\epsilon(\boldsymbol{u} \cdot \nabla)\boldsymbol{u} - \nabla\eta + \frac{\delta^2}{3}\nabla q, \tag{B11}$$

$$\frac{\delta^2}{3}\nabla \cdot (\nabla q) - q = \nabla \cdot [\epsilon(\boldsymbol{u} \cdot \nabla)\boldsymbol{u} + \nabla\eta]\,. \tag{B12}$$

At each time step, the auxiliary equation (B12) is inverted to find q, which can be efficiently done in Fourier space; see Steinmoeller *et al.* (2012) for details. The data for q is then used in the simultaneous time stepping of (B10) and (B11).

The KdVθ equation has the form

$$\mu_1 A_T + \mu_2 A A_\xi + \mu_3 A_{\xi\xi\xi} + \mu_5 \frac{A_\theta}{T} = 0. \tag{B13}$$

Applying the 2-D discrete Fourier transform yields

$$\hat{A}_T = -\frac{ik_\xi \mu_2}{2\mu_1}\mathcal{F}[A^2] + \frac{ik_\xi^3 \mu_3}{\mu_1}\hat{A} - \frac{ik_\theta \mu_5}{\mu_1}\frac{\hat{A}}{T}, \tag{B14}$$

which is then efficiently iterated in time using the RK4 algorithm discussed above. One must choose the values of T to not include zero to avoid division by zero, similar to the values at the origin for $R = 0$ for the radial case.

To discretise and numerically solve the KPII equation, we follow the method presented by Klein *et al.* (2007), Biondini *et al.* (2025). To account for both the inward- and outward-propagating versions, we rewrite the KPII equation as

$$\left(2\eta_T + \frac{3\sigma}{2}(\eta^2)_\xi + \frac{\sigma}{3}\eta_{\xi\xi\xi}\right)_\xi + \sigma\eta_{YY} = 0, \tag{B15}$$

where σ is 1 or -1 for the right/left-propagating case, respectively, and $\xi = x - \sigma t$. Applying the 2-D Fourier transform to (B15) and rearranging gives

$$\hat{\eta}_T = -\frac{3\sigma i k_\xi}{4}\mathcal{F}[\eta^2] + \frac{\sigma i k_\xi^3}{6}\hat{\eta} - \frac{\sigma i k_Y^2}{2k_\xi}\hat{\eta}. \tag{B16}$$

It is noted that the form of (B16) includes division by zero for the zero wavenumber in k_ξ, however, this relates to the zero-mass condition of the KPII equation. If the zero-mass condition is satisfied at T_0 then there is no growth in the zero mode for all T^n, and so it is satisfactory to remove the mass from the initial condition and at each time step set $\hat{\eta}(T^n, 0, k_Y) = 0$; see Klein *et al.* (2007), Biondini *et al.* (2025) and the references therein

https://doi.org/10.1017/jfm.2025.10934 Published online by Cambridge University Press

for details. Due to the form of (B16), it is convenient to introduce the integrating factor

$$\Lambda = \exp\left(-\sigma i\left(\frac{k_\xi^3}{6} - \frac{k_Y^2}{2k_\xi}\right)T\right), \tag{B17}$$

such that $\hat{q} = \Lambda\hat{\eta}$. Substituting this expression for $\hat{\eta}$ into (B16) removes the stiff terms from the problem, and we obtain

$$\hat{q}_T = -\frac{3\sigma i k_\xi \Lambda}{4}\mathcal{F}[\eta^2], \tag{B18}$$

which is a simple ODE for $\hat{q}$. At each time step, we calculate η^n from $\hat{q}^n = \Lambda\hat{\eta}^n$ and then calculate $\hat{q}^{n+1}$. For the KPII equation, performing additional Fourier transforms to invert the integrating factor is still computationally more efficient than solving the original stiff problem.

Appendix C. Reduction to the KdV equation

For plane surface and internal waves co-propagating with a shear flow, it can be shown that the amplitude (3.3) reduces to the previously known KdV equation (see, for example, Grimshaw 2005 evaluated for the case of a flat bottom). Indeed, for the waves co-propagating with the current, the general solution is $k = a\cos\theta$ and $\xi = rk(\theta) - st = a(x - \hat{s}t)$, where we have scaled $s \to a\hat{s}$. The modal equations (1.3)–(1.5) reduce to

$$\left[\rho_0(u_0 - \hat{s})^2\phi_z\right]_z - \rho_{0z}\phi = 0 \quad \text{for} \quad 0 < z < 1, \tag{C1}$$

$$(u_0 - \hat{s})^2\phi_z - \phi = 0 \quad \text{at} \quad z = 1, \tag{C2}$$

$$\phi = 0 \quad \text{at} \quad z = 0. \tag{C3}$$

Scaling $\xi = rk(\theta) - st = a(x - \hat{s}t)$ to become $\hat{\xi} = x - \hat{s}t$, assuming that $A_\theta = 0$ (there is no change in the tangential direction along the wavefront) and computing the remaining coefficients in (3.3) we obtain

$$I_1 A_T + I_2 A A_{\hat{\xi}} + I_3 A_{\hat{\xi}\hat{\xi}\hat{\xi}} = 0, \tag{C4}$$

where $T = \epsilon t$, $\hat{\xi} = x - \hat{s}t$ and

$$I_1 = 2\int_0^1 \rho_0(u_0 - \hat{s})\phi_z^2\,\mathrm{d}z, \quad I_2 = -3\int_0^1 \rho_0(u_0 - \hat{s})^2\phi_z^3\,\mathrm{d}z, \tag{C5}$$

$$I_3 = -\int_0^1 \rho_0(u_0 - \hat{s})^2\phi^2\,\mathrm{d}z. \tag{C6}$$

The amplitude equation (C4) and coefficients (C5) and (C6) match those of Grimshaw (2005) identically.

The amplitude equation for obliquely propagating plane waves was given by Miles (1977). This equation can also be recovered from (3.3) for $\hat{\xi} = x + b(a)y/a - \hat{s}t$. It has the form of (C4), where the coefficients are given by

$$I_1 = 2\int_0^1 \rho_0(u_0 - \hat{s})\phi_z^2\,\mathrm{d}z, \quad I_2 = -3\int_0^1 \rho_0(u_0 - \hat{s})^2\phi_z^3\,\mathrm{d}z, \tag{C7}$$

$$I_3 = -\frac{[a^2 + b(a)^2]}{a^2}\int_0^1 \rho_0(u_0 - \hat{s})^2\phi^2\,\mathrm{d}z, \tag{C8}$$

https://doi.org/10.1017/jfm.2025.10934 Published online by Cambridge University Press

and the modal equations have the form

$$\left[\frac{\rho_0 a^2(u_0-\hat{s})^2}{a^2+b(a)^2}\phi_z\right]_z-\rho_{0z}\phi=0 \quad \text{for} \quad 0<z<1, \tag{C9}$$

$$\frac{a^2(u_0-\hat{s})^2}{a^2+b(a)^2}\phi_z-\phi=0 \quad \text{at} \quad z=1, \tag{C10}$$

$$\phi=0 \quad \text{at} \quad z=0. \tag{C11}$$

The modal equations (C9)–(C11) reduce to (C1)–(C3) when the wave is co-propagating with the current, since in this case $b(a)=0$.

References

Ablowitz, M. & Baldwin, D. 2012 Nonlinear shallow ocean-wave soliton interactions on flat beaches. *Phys. Rev. E* **86**, 036305.

Ablowitz, M. & Curtis, S. 2013 Conservation laws and non-decaying solutions for the Benney–Luke equation. *Proc. R. Soc. A* **469**, 20120690.

Ablowitz, M. & Segur, H. 1979 On the evolution of packets of water waves. *J. Fluid Mech.* **92**, 691–715.

Apel, J. 2003 A new analytical model for internal solitons in the ocean. *J. Phys. Oceanogr.* **33**, 2247–2269.

Apel, J., Ostrovsky, L., Stepanyants, Y. & Lynch, J. 2007 Internal solitons in the ocean and their effect on underwater sound. *J. Acoust. Soc. Am.* **121**, 695–722.

Barros, R. & Choi, W. 2014 Elementary stratified flows with stability at low Richardson number. *Phys. Fluids* **26**, 124107.

Bassi, C., Bonaventura, L., Busto, S. & Dumbser, M. 2020 A hyperbolic reformulation of the Serre–Green–Naghdi model for general bottom topographies. *Comput. Fluids* **212**, 104716.

Biondini, B., Bivolcic, A. & Hoefer, M. 2025 Mach reflection and expansion of two-dimensional dispersive shock waves. *Phys. Rev. Lett.* **135**, 067201.

Biondini, G., Hoefer, M. & Moro, A. 2020 Integrability, exact reductions and special solutions of the KP–Whitham equations. *Nonlinearity* **33**, 4114–4132.

Bona, J., Lannes, D. & Saut, J. 2008 Asymptotic models for internal waves. *J. Math. Pure Appl.* **89**, 538–566.

Boonkasame, A. & Milewski, P. 2011 The stability of large-amplitude shallow interfacial non-Boussinesq flows. *stud. Appl. Math.* **133**, 182–213.

Burns, J.C. 1953 Long waves in running water. *Proc. Camb. Phil. Soc.* **49**, 695–706.

Chakravarty, S. & Kodama, Y. 2009 Soliton solutions of the KP equation and application to shallow water waves. *Stud. Appl. Math.* **123**, 83–151.

Chakravarty, S. & Kodama, Y. 2014 Construction of KP solitons from wave patterns. *J. Phys. A* **47**, 025201.

Chakravarty, S., Lewkow, T. & Maruno, K. 2010 On the construction of the KP line-solitons and their interactions. *Appl. Anal.* **89**, 529–545.

Chwang, A. & Wu, T. 1977 *Cylindrical Solitary Waves, Waves On Water of Variable Depth*. Springer.

Dorfman, A., Pelinovsky, E. & Stepanyants, Y. 1981 Finite-amplitude cylindrical and spherical waves in weakly dispersive media. *Sov. Phys. J. Appl. Mech. Tech. Phys.* **2**, 206–211.

Drazin, P. 1983 *Solitons London Mathematical Society Lecture Note Series*. Cambridge University Press.

Durykh, D., Clamind, D., Milewski, P. & Mitsotakis, D. 2013 Finite volume and pseudospectral schemes for the fully nonlinear 1D Serre equations. *Eur. J. Appl. Math.* **24**, 761–787.

Ellingsen, S. 2014*a* Ship waves in the presence of uniform vorticity. *J. Fluid Mech.* **742**, R2.

Eskilsson, C. & Sherwin, S. 2006 Spectral/hp discontinuous Galerkin methods for modelling 2D Boussinesq equations. *J. Comput. Phys.* **212**, 566–589.

Gardner, C., Green, J., Kruskal, M. & Miura, R. 1967 Method for solving the Korteweg–de Vries equation. *Phys. Rev. Lett.* **19**, 1095–1097.

Gavrilyuk, S. & Klein, C. 2024 Numerical study of the Serre–Green–Naghdi equations in 2D. *Nonlinearity* **37**, 045014.

Gavrilyuk, S. & Shyue, K. 2024 2D Serre–Green–Naghdi equations over topography: elliptic operator inversion method. *J. Hydraulic Engng* **150**, 04023054.

Grimshaw, R. 2005 *Nonlinear Waves in Fluids: Recent Advances and Modern Applications*. Springer.

Grimshaw, R., Helfrich, K. & Johnson, E. 2013 Experimental study of the effect of rotation on large amplitude internal waves. *Phys. Fluids* **25**, 056602.

https://doi.org/10.1017/jfm.2025.10934 Published online by Cambridge University Press

GRIMSHAW, R., OSTROVSKY, L., SHRIRA, V. & STEPANYANTS, Y. 1998 Long nonlinear surface and internal gravity waves in a rotating ocean. *Surv. Geophys.* **19**, 289–338.
GRIMSHAW, R., PELINOVSKY, E., TALIPOVA, T. & KURKINA, O. 2010 Internal solitary waves: propagation, deformation and disintegration. *Nonlin. Proc. Geophys.* **17**, 633–649.
GRUE, J. 2006 Very large internal waves in the ocean – observations and nonlinear models. In *Waves in Geophysical Fluids* (ed. J. Grue & K. Trulsen), pp. 1–66. Springer.
HARAGUS, M., LI, J. & PELINOVSKY, D. 2017 Counting unstable eigenvalues in Hamiltonian spectral problems via commuting operators. *Comm. Math. Phys.* **354**, 247–268.
HE, Y. & CHABCHOUB, A. 2025 On long-crested ocean rogue waves originating from localized amplitude and frequency modulations. *Ocean Model.* **193**, 102464.
HELFRICH, K. & MELVILLE, W. 2006 Long nonlinear internal waves. *Ann. Rev. Fluid Mech.* **38**, 395–425.
HOOPER, C., KHUSNUTDINOVA, K. & GRIMSHAW, R. 2021 Wavefronts and modal structure of long surface and internal ring waves on a parallel shear current. *J. Fluid Mech.* **927**, A37.
HORNICK, J., PELINOVSKY, D. & SCHNEIDER, G. 2025 On the long-wave approximation of solitary waves in cylindrical coordinates. *Nonlinear Differ. Equ. Appl.* **32**, 50.
HU, L., LUO, X. & WANG, Z. 2025 Obliquely interacting solitary waves and wave wakes in free-surface flows. *J. Fluid Mech.* **1011**, A8.
JOHNSON, R. 1990 Ring waves on the surface of shear flows: a linear and nonlinear theory. *J. Fluid Mech.* **215**, 145–160.
JOHNSON, R. 1997 *A Modern Introduction to the Mathematical Theory of Water Waves*. Cambridge University Press.
JOHNSON, R. 1999 A note on an asymptotic solution of the cylindrical Korteweg-de Vries equation. *Wave Motion* **30**, 1–16.
KADOMTSEV, B. & PETVIASHVILI, V. 1970 On the stability of solitary waves in weakly dispersing media. *Soviet Phys. Doklady* **15**, 539–541.
KATSAOUNIS, T., MITSOTAKIS, D. & SADAKA, G. 2020 Boussinesq–Peregrine water wave models and their numerical approximation. *J. Comput. Phys.* **417**, 109579.
KHARIF, C., PELINOVSKY, E. & SLUNYAEV, A. 2008 *Rogue Waves in the Ocean, Advances in Geophysical and Environmental Mechanics and Mathematics*. Springer.
KHORBATLY, B. & KALISCH, H. 2024 Rigorous estimates on mechanical balance laws in the Boussinesq–Peregrine equations. *Stud. Appl. Math.* **152**, 847–867.
KHUSNUTDINOVA, K. 2020 Long internal ring waves in a two-layer fluid with an upper-layer current. *Russ. J. Earth Sci.* **20**, ES4006.
KHUSNUTDINOVA, K. & ZHANG, X. 2016*a* Long ring waves in a stratified fluid over a shear flow. *J. Fluid Mech.* **794**, 17–44.
KIVSHAR, Y. & PELINOVSKY, D. 2000 Self-focusing and transverse instabilities of solitary waves. *Phys. Rep.* **331**, 117–195.
KLEIN, C., SPARBER, C. & MARKOWICH, P. 2007 Numerical study of oscillatory regimes in the Kadomtsev–Petviashvili equation. *J. Nonlinear Sci.* **17**, 429–470.
KO, K. & KUEL, H. 1979 Cylindrical and spherical KdV solitary waves. *Phys. Fluids* **22**, 1343–1348.
KRECHETNIKOV, R. 2024 Transverse instability of concentric water waves. *J. Nonlinear Sci.* **34**, 66.
LAMB, K. 2005 *Extreme Internal Solitary Waves in the Ocean: Theoretical Considerations*. Aha Huliko'a Hawaiian Winter Workshop.
LANDAU, L. & LIFSHITZ, E. 1959 *Quantum Mechanics*. Pergamon Press.
LANNES, D. 2020 Modelling shallow water waves. *Nonlinearity* **33**, R1.
LANNES, D. & MING, M. 2015 The Kelvin–Helmholtz instabilities in two-fluids shallow water models. In *Hamiltonian Partial Differential Equations and Applications, Fields Institute Comms*, vol. 75, Springer.
LI, Y. & ELLINGSEN, S. 2019 A framework for modelling linear surface waves on shear currents in slowly varying waves. *J. Geophys. Res.: Oceans* **124**, 2527–2545.
MILES, J. 1977 Obliquely interacting solitary waves. *J. Fluid Mech.* **79**, 157–169.
MILES, J. 1978 An axisymmetric Boussinesq wave. *J. Fluid Mech.* **84**, 181–191.
MIZUMACHI, T. 2015 Stability of line solitons for the KP-II equation in R2. *Mem. Am. Math. Soc.* **238**, 1125.
MIZUMACHI, T. & SHIMABUKURO, Y. 2017 Asymptotic linear stability of Benney-Luke line solitary waves in 2D. *Nonlinearity* **30**, 3419–3465.
MIZUMACHI, T. & SHIMABUKURO, Y. 2020 Stability of Benney-Luke line solitary waves in 2 dimensions. *SIAM J. Math. Anal.* **52**, 4238–4283.
MIZUMACHI, T. & TZVETKOV, N. 2012 Stability of the line soliton of the KP-II equation under periodic transverse perturbations. *Math. Ann.* **352**, 659–690.

https://doi.org/10.1017/jfm.2025.10934 Published online by Cambridge University Press

NIRUNWIROJ, K., TSELUIKO, D. & KHUSNUTDINOVA, K. 2025 Evolution of internal cnoidal waves with local defects in a two-layer fluid with and without rotation. *J. Fluid Mech.* **1023**, A26.

ONORATO, M., RESIDORI, S., BORTOLOZZO, U., MONTINA, A. & ARECCHI, F. 2013 Rogue waves and their generating mechanisms in different physical contexts. *Phys. Rep.* **528**, 47–89.

OSTROVSKII, L., PELINOVSKY, E., SHRIRA, V. & STEPANYANTS, Y. 2015 Beyond the KdV: post-explosion development. *Chaos* **25**, 097620.

OSTROVSKII, L. & SHRIRA, V. 1976 Instability and self-refraction of solitons. *Sov. J. Exp. Theor. Phys* **44**, 738–743.

OVSYANNIKOV, L. 1979 Two-layer "shallow-water" model. *J. Appl. Math. Tech. Phys.* **20**, 127–135.

PEREGRINE, D. 1967 Long waves on a beach. *J. Fluid Mech.* **27**, 815–827.

PESENSON, M. 1991 Nonlinear waves travelling upon a front of solitons. *Phys. Fluids* **3**, 3001–3006.

PORUBOV, A., TRUJI, H., LAVRENOV, I. & OIKAWA, M. 2005 Formation of the rogue wave due to non-linear two-dimensional waves interaction. *Wave Motion* **42**, 202–210.

RYSKAMP, S., HOEFER, M. & BIONDINI, G. 2022 Modulation theory for soliton resonance and Mach reflection. *Proc. R. Soc. A* **478**, 20210823.

RYSKAMP, S., MAIDEN, M., BIONDINI, G. & HOEFER, M. 2021 Evolution of truncated and bent gravity wave solitons: the Mach expansion problem. *J. Fluid Mech.* **909**, A24.

SHRIRA, V. & PESENSON, M. 1984 Soliton stability with respect to transverse perturbations of finite length and amplitude. *Nonlinear Turbulent Process. Phys.*1061–1068.

SIDOROVAS, N., TSELUIKO, D., CHOI, W. & KHUSNUTDINOVA, K. 2024 Nonlinear concentric water waves of moderate amplitude. *Wave Motion* **128**, 103295.

SIDOROVAS, N., TSELUIKO, D., CHOI, W. & KHUSNUTDINOVA, K. 2025 Internal solitary and cnoidal waves of moderate amplitude in a two-layer fluid: the extended KdV equation approximation. *Phys. D* **481**, 134723.

SLUNYAEV, A. & PELINOVSKY, E. 2016 Role of multiple soliton interactions in the generation of rogue waves: the modified Korteweg-de Vries framework. *Phys. Rev. Lett.* **117**, 214501.

SMELTZER, B., ÆSØY, E. & ELLINGSEN, S. 2019 Observation of surface wave patterns modified by sub-surface shear currents. *J. Fluid Mech.* **873**, 508–530.

STASTNA, M. 2022 *Internal Waves in the Ocean: Theory and Practice*. Springer.

STEINMOELLER, D., STASTNA, M. & LAMB, K. 2012 Fourier pseudospectral methods for 2D Boussinesq-type equations. *Ocean Model.* **52**, 76–89.

TREFETHEN, L. 2000 Spectral methods in MATLAB, software, environments, tools. SIAM.

TSELUIKO, D., ALHARTHI, N., BARROS, R. & KHUSNUTDINOVA, K. 2023 Internal ring waves in a three-layer fluid on a current with a constant vertical shear. *Nonlinearity* **36**, 3431–3466.

YUAN, C., GRIMSHAW, R., JOHNSON, E. & WANG, Z. 2018 Topographic effect on oblique internal wave–wave interactions. *J. Fluid Mech.* **836**, 36–60.

YUAN, C. & WANG, Z. 2022 On diffraction and oblique interactions of horizontally two-dimensional internal solitary waves. *J. Fluid Mech.* **936**, A20.

ZHANG, Z., HU, W., GUO, Q. & STEPANYANTS, Y. 2024 Solitons and lumps in the cylindrical Kadomtsev–Petviashvili equation. II. Lumps and their interactions. *Chaos* **34**, 013132.

https://doi.org/10.1017/jfm.2025.10934 Published online by Cambridge University Press